Journal Pre-proof

How petrophysical properties influence the seismic signature of carbonate fault damage zone: Insights from forward-seismic modelling

Andrea Tomassi, Fabio Trippetta, Roberto de Franco, Roberta Ruggieri

PII: S0191-8141(23)00019-6

DOI: https://doi.org/10.1016/j.jsg.2023.104802

Reference: SG 104802

To appear in: *Journal of Structural Geology*

Received Date: 27 July 2022

Revised Date: 11 January 2023

Accepted Date: 14 January 2023

Please cite this article as: Tomassi, A., Trippetta, F., de Franco, R., Ruggieri, R., How petrophysical properties influence the seismic signature of carbonate fault damage zone: Insights from forward-seismic modelling, *Journal of Structural Geology* (2023), doi: https://doi.org/10.1016/j.jsg.2023.104802.

How petrophysical properties influence the seismic signature of carbonate fault damage zone: insights from forward-seismic modelling

Andrea Tomassi[1]*, Fabio Trippetta[1], Roberto de Franco[2], Roberta Ruggieri[1]

1 - Department of Earth Sciences, Sapienza University of Rome, Piazzale Aldo Moro, 5, 00185 Roma, Italy

2 - Istituto di Geologia Ambientale e Geoingegneria, CNR, Via Mario Bianco, 9, 20131 Milano, Italy

* - Corresponding author: Andrea Tomassi (email: andrea.tomassi@uniroma1.it; phone: +393887628764; permanent address: Piazzale Aldo Moro, 5, 00185 Roma, Italy)

Fabio Trippetta: fabio.trippetta@uniroma1.it

Roberto de Franco: roberto.defranco@igag.cnr.it

Roberta Ruggieri: roberta.ruggieri@uniroma1.it

Keywords: Geophysical modelling; Petrophysics; Forward modelling; Synthetic seismic

Abstract

Seismic imaging is the most common tool to detect subsurface structures in continental and marine settings. Despite technological advancement, seismic analysis of carbonates is still challenging because they are strongly influenced by petrophysical heterogeneities, being this even more difficult when further heterogeneities are added by the presence of faults. In this work, unmigrated forward-seismic models are developed to understand the seismic response changes related to carbonate-bearing fault systems and their deformation behaviour. We focus on the carbonate ramp of the Majella Massif (central Italy), that is characterised by the presence of porous and faulted carbonate lithologies. This carbonate system represents an analogue of carbonate reservoirs worldwide. Field and laboratory data of fault rocks sampled at increasing distances from the slip planes highlight a damage zone/fault core architecture with a decreasing porosity approaching fault planes. This observation is also confirmed by the thin sections analysis and the calculation of the shear modulus. Seismic images of fault rocks presenting lower porosity than the host rock show weak diffraction hyperbolas while diffraction hyperbolas are more evident in the forward-seismic models of fault rocks with greater porosity than the host rock. Moreover, factors such as the variation in the dip angle of the fault or the thickness of the damage zone can enhance or reduce the hyperbolas. Performing the migration process to stacked sections would not provide evidence of increased porosity in the damage zone due to the suppression of the diffractive component. The presence of weak hyperbolas in unmigrated seismic images is thus interpreted as evidence of a lower porosity damage zone with respect to the host rock. This can be related to deformation mechanisms leading to porosity loss in the damage zone for porous rocks as observed in the study area. However, this could also be related to the confining stress or fracture filling that counteract the fracture-related porosity increase when faults are hosted by tight rocks.

1. Introduction

Geophysical surveys performed in carbonate ramp systems are difficult to interpret because of their strong facies heterogeneity (Palaz and Marfurt, 1997; Tomassi et al., 2022). Further complications are then related to the presence of faults (Botter et al., 2014; Faleide et al., 2021), which can have very different effects on the seismic response of carbonate rocks (Wang et al., 1997). Carbonate-bearing faults are usually characterised by one or more slip zones (the fault core), surrounded by a region characterised by fractures, joints, veins, shear bands or deformation bands (damage zone) (Caine et al., 1996; Trippetta et al., 2017). The petrophysical characterisation of the transition from the fault core to the damage zone is not simple to perform (Hadizadeh and Rutter, 1983), especially in carbonate rocks (Billi et al, 2003).

Fault-related deformation generates higher fracture density within the fault damage zone with respect to the surrounding host rocks, thus deformation in the damage zone decreases moving from the fault core toward the undeformed host rocks (e.g., Caine et al., 1996; Smeraglia et al., 2014; Trippetta et al., 2017; Mayolle et al., 2019; Volatili et al., 2022). For small displacement faults, damage is represented by different structures such as fractures and/or deformation bands, which frequency depends on displacement (Mayolle et al., 2019) and stress distribution (Mercuri et al., 2020; Volatili et al., 2022). The lithologies belonging to both the fault core and to the damage zone have different petrophysical characteristics because they experienced distinct stress and strain conditions influenced by the fault slip behaviour (Wibberley et al., 2008; Michie, 2015; Michie and Haines, 2016). These dynamics cause the fault rocks to have different elastic parameters with respect to the protolith and thus different acoustic impedances with respect to the surrounding rocks (Botter et al., 2014; Faleide et al., 2021). Fault zones from shallow-water carbonate rocks are characterised by variable brittle deformation modes (Caine et al., 1996; Tondi et al., 2006; Antonellini et al., 2008; Agosta et al., 2009; Agosta et al., 2010; Giorgioni et al., 2011; Agosta et al., 2012; Trippetta et al., 2017). In these lithologies, faulting could be often associated with opening mode fractures (Mollema and Antonellini, 1996). However, carbonate dissolution allows the development of pressure solution and the subsequent shearing of solution surfaces (Mollema and Antonellini, 1996; Storti et al., 2007; Antonellini et al., 2008; Rustichelli et al., 2012). These processes combined with microcracking and grain comminution (Baud et al., 2004; Wong and Baud, 2009; Heap et al., 2015; Fossen, 2016) lead to the generation of cataclastic bands and solution and cementation bands. These structures are associated with porosity reduction due to pore collapse and grain comminution and are generally characterized as deformation bands (Fossen, 2016). The resulting geometry and architecture of the fault zones strongly influence the seismic images of the carbonate-bearing fault zones. Forward modelling can thus help in obtaining evidence about the seismic response of fault rocks particularly if the petrophysical changes from the host rock to the fault planes can be properly constrained. Various forward seismic modelling techniques are adopted over the years to accurately represent the subsurface (Carcione et al., 2002). The point-spread function (PSF) convolution modelling (Wrona et al., 2020; Jensen et al., 2021) applies a 2-D convolution operator to the reflectivity model through the wavelet and its frequency, velocity, angle of incidence and illumination patterns that determine which parts of a geological structure are imaged by controlling lateral resolution (Lecomte et al., 2016; Wrona et al., 2020). The finite element method (FEM) (Aagaard et al., 2001; Bielak et al., 2003) is based on non-structured grids and thus involves more elaborate preparation steps. The global pseudo-spectral methods (GPSM) are based on Fourier interpolation or Chebyshev interpolation (Kosloff & Baysal 1982; Kosloff et al., 1990), based on a structured grid with global spectral differential operators (Klin et al., 2010). The finite difference method (FDM) (Bohlen 2002; Moczo et al., 2007), discretizes the computational domain across a grid making use of spatial operators and it is particularly suitable to simulate complex geological structures. In this work we used the FDM starting with a very detailed petrophysical characterisation of the involved structures derived from natural carbonate fault rocks (Tondi, 2007; Matonti et al., 2012; Michie et al., 2016; Trippetta and Geremia, 2019; Trippetta et al., 2020). Such petrophysical characterisation provides input data to conduct an in-depth analysis of the unmigrated seismic modelling outputs related to carbonate-bearing faults.

2. Geological setting

This work focuses on fault zones set up in the shallow-water carbonate ramp outcropping on the northern portion of the Majella Massif, central Italy (Figure 1). Platform carbonates outcrop in the central and southern portions of the Majella Massif while the northern portion exposes a Cretaceous-to-Miocene carbonate ramp. This latter is considered a great analogue of carbonate reservoirs, exploited in the offshore Adriatic Sea and also in other regions worldwide (Tomassetti et al., 2021). Accordingly, several natural heavy-hydrocarbon impregnations are found in the NW sectors of the area, especially within the Miocene carbonate formations (Lipparini et al., 2018). The Majella Massif is a N-S and NW-SE oriented thrust-related, box-shaped non-cylindrical anticline structure plunging both to the North and South (Vezzani and Ghisetti, 1998; Patacca et al., 2008; Agosta et al., 2009; Bianchi Fasani et al., 2011; Cornacchia et al., 2017). The structural evolution of the Majella area can be divided into five main phases: 1) Cretaceous extension evidenced by NNW–SSE oriented normal faults (Accarie et al., 1986; Casabianca et al., 2002; Di Cuia et al., 2009); 2) Miocene-Pliocene new extensional phase recorded in the flexural extensions of the Apulian plate in westward subduction (Scisciani et al., 2002; Rustichelli et al., 2016); 3) Pliocene compressional phase evidenced by folding and thrusting due to the Europe-Africa continental collision that allowed the formation of the Majella anticline (Tondi et al., 2006; Antonellini et al., 2008; Agosta et al., 2009; Aydin et al., 2010; Rustichelli et al., 2016); 4) Quaternary subsequent collapse of the thrust wedge (Ghisetti and Vezzani, 2002; Rustichelli et al., 2016); 5) Pleistocene-Holocene extension active to the south of the area (Pizzi et al., 2010; Rustichelli et al., 2016). The lithologies characterizing the stratigraphic succession of the northern portion of the Majella are mainly limestones ranging from Jurassic to Upper Miocene in age (Brandano et al., 2016). During the Mesozoic, a northward-increasing slope developed, successively covered by shallow-water carbonates sediments (Vecsei et al., 1998). From the Campanian, the Orfento Formation (ORF) has prograded on the slope (Rusciadelli et al., 2003; Rusciadelli and Ricci, 2008) being then overlaid by the Paleocene to Eocene Santo Spirito Formation (SS). The Bolognano Formation deposited from the Oligocene to Miocene and is characterised by five different lithological members (Mutti et al., 1997, 1999; Brandano et al., 2012, 2016) that are from bottom to top: 1. Lepidocyclina Limestones 1 (LP1), 2. Cherty and Marly limestone member (CM), 3. Lepidocyclina Limestones 2 member (LP2), 4. Hemipelagic Marls member (HM), 5. Lithothamnion Limestone (LL). Above the Bolognano Fm. in the Messinian occurred the deposition of the Gessoso-Solfifera Formation (Crescenti et al., 1969). The Plio-Quaternary evolution of the massif was characterised by the persistence of a continental depositional environment (Cosentino et al., 2010; Bianchi Fasani et al., 2011).

The orientation of the fault planes and fractures present on the Majella Massif is determined by the tectonic phases recorded in the carbonate succession. In the Late

Cretaceous, ENE-WSW oriented extension causes normal faults with NNW-SSE and NNW-SSE trends (Accarie and Beaudoin, 1988; Casabianca et al., 2002). During the late Miocene, a NE-SW oriented extension is recorded connected to the westward subduction of the Apulian plate generating NW-SE trending normal faults (Agosta et al., 2006, 2009; Di Cuia et al., 2009). During the Pliocene, the Europe-Africa continental collision resulted in the E-W oriented folding with the build-up of large anticlines such as the Majella massif. In the Plio-Pleistocene, tectonics is characterised by movements along normal faults with a strike-slip component recorded in the carbonate succession by the evident NE-SW to NW-SE oriented fault systems (Di Cuia et al., 2009). The faults studied in this paper are associated with these latter stages of the geodynamic evolution and outcrop in the east, central and north-west sectors of the Majella Mountain (Figure 1).

The first analysed fault in this work is the Piano delle Cappelle fault (named PDC in Figure 1), which is almost 8 km long and is hosted in the Bolognano Formation striking N150° and dipping 60° to SW. This is a regional fault with a normal component of slip (Tomassetti et al, 2021) and with a total displacement of 240 m.

The second investigated fault, which has a length of 1 km, is hosted in the Bolognano Formation and outcrops close to Decontra village striking N200° and dipping 56° to S (named DE LP in Figure 1). Kinematic indicators highlight oblique-normal faulting slip with a total displacement ranging from tens of centimetres to one metre.

The third examined fault with a length of 750 m, is hosted in the Orfento Formation and outcrops close to Pennapiedimonte village striking N40° and dipping 90° (named PE ORF in Figure 1). Kinematic indicators, such as slickenlines and mineral (calcite) growth, show that the PE ORF fault is characterised by transtentional slip with a total displacement from a few centimetres to tens of centimetres.

The last analysed fault with a length of 2 km, is hosted in the Santo Spirito Formation and outcrops in the Santo Spirito Valley striking N220° and dipping 68° to SW (Figure 1 FS SS). Kinematic indicators mainly suggest normal slip and the total displacement is on the order of a few metres.

In the sampling areas, all analysed faults are intraformational and therefore displacements do not cause structural contacts between different formations. From the field analysis, the studied faults show a classic architecture pattern characterised by a centimetric fault core, where most of the deformation accumulates, and a damage zone of a few tens of metres where the deformation gradually decreases towards the host rock (Caine et al., 1996; Fossen, 2016). It should be noted that in the damage zone belonging to the analysed faults, no major fracture systems are appreciable at the outcrop scale.

On the other hand, several fault outcroppings in the Majella area are characterised by high fracturing with an increased porosity within the damage zone (Marchegiani et al., 2006; Pisani et al., 2021), allowing fluid flow (Romano et al., 2017) especially in the Bolognano Formation outcrops of the Roman Quarry close to Lettomanoppello village (Figure 1) (Agosta et al., 2009; Giorgioni et al., 2009; Volatili et al., 2019; Zambrano et al., 2021).

Regardless of the architecture of the fault zone (fractured or not), field observations and literature data (Agosta et al., 2009; Giorgioni et al., 2009; Romano et al., 2020) suggest that, on average, the damage zones of all the faults outcropping in the Majella area show a maximum width of 50 m; beyond that distance, no deformations are generally appreciable at the outcrop scale.

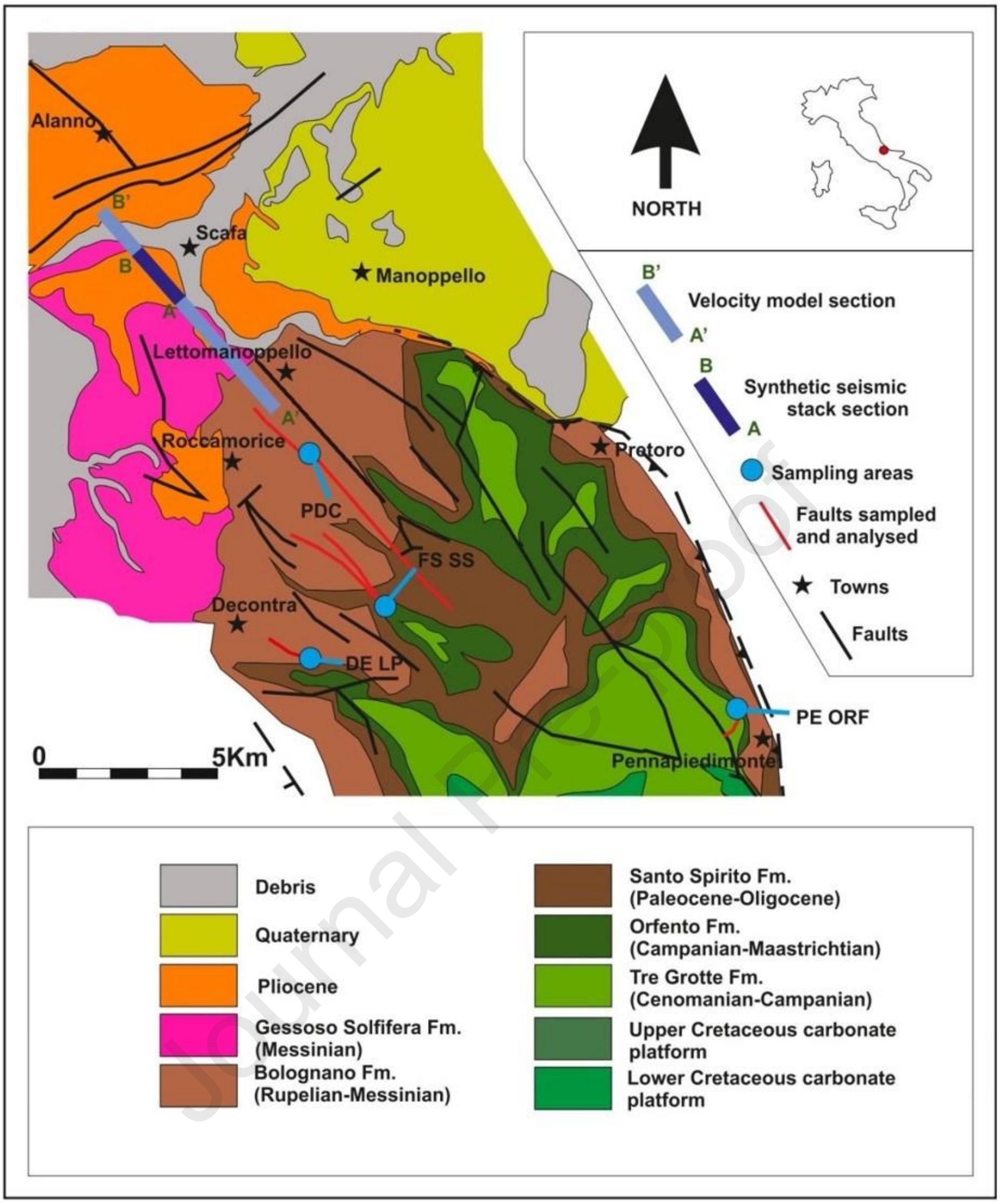

Figure 1. Geologic sketch of the Majella Massif (modified after Tomassi et al., 2022, and Trippetta et al., 2021) reporting sampling locations (cyan dots), sampled faults (drawn in red), and location of the velocity model section and the synthetic seismic section produced in this work and represented with a light blue line and a blue line, respectively.

3. Methods

3.1 Fieldwork and sampling

Fieldwork revealed that all the analysed fault zones are characterised by the classical fault core - damage zone - host rock architecture (Caine et al., 1996; Fossen, 2016). Since the focus was on small-displacement faults, at the outcrop scale fault cores were not clearly detectable, however they are usually characterised by highly compacted rocks with a maximum width of 10 cm (Tondi et al., 2006; Agosta et al., 2009; Giorgioni et al., 2009; Romano et al., 2020) close to the main fault plane. Moreover, rocks belonging to the fault core show frequent calcite veins and stylolite clearly visible at the thin section scale (see par. 4.1 Thin section analysis). Rocks related to the damage zones show deformation bands (Caine et al., 1996; Fossen, 2016) and small fractures mainly randomly oriented. At distance larger than 50 m from the main slip plane, no evident deformation features are observed in agreement with literature studies on similar faults (Tondi et al., 2006; Agosta et al., 2009; Giorgioni et al., 2009; Romano et al., 2020).

Following these observations, samples were collected at progressive distances from the main fault plane: 1) fault core samples were collected at distances of less than 10 cm; 2) damage zone samples were collected at distances between 10 cm and 50 m; 3) host rock samples were collected at a distance greater than 50 m. Sampling was carried out on the Piano delle Cappelle fault (Figure 1 PDC), on the fault outcropping close to Decontra village (Figure 1 DE LP), on the fault close to Pennapiedimonte village (Figure 1 PE ORF) and the fault outcropping in the Santo Spirito Valley (Figure 1 FS SS).

3.2 Laboratory measurements

Density and porosity measurements were carried out with a helium pycnometer (Anton Paar instruments). Bulk density was calculated from sample weight divided by sample volume. The mathematical difference between the geometrical volume of the sample, measured with a calibre, and the volume measured by the pycnometer divided by the geometric volume allowed to calculate the connected porosity (Ruggieri and Trippetta, 2020; Trippetta et al., 2020).

The seismic velocity of samples (P-wave, Vp and S-wave, Vs) have been calculated by using the USB8M ultrasonic device generator (Mistras Eurosonic) connected to two piezoelectric transducers. The transducers were positioned at the top and bottom of each sample for the measurements. One transducer acted as a transmitter, and the waveforms were registered with an equal receiving transducer. Waveforms were then handled with the USB8M ultrasonic device generator to manage the signal. Signals were displayed with the software provided which allowed to pick the first arrivals of the waves. Then, velocity was calculated as the ratio between the length of each sample and the first Vp and Vs waves arrivals. All laboratory measurements have been performed at the Rock Mechanics and Earthquake Physics laboratory of the Sapienza Earth Sciences department.

Vp was the fundamental parameter on which the seismic modelling was designed, while density and Vs measurements were required to calculate the acoustic impedances and then the shear modulus values and providing a rheological contribution to the characterisation of the fault systems analysed in this work.

4. Samples characterisation

4.1 Thin section analysis

From the fault rock samples, 34 thin sections were realized to identify microstructures related to faulting (Figure 2). The thin sections analysis confirms the field observations, i.e., the studied faults show a classical model where there is the presence of a thin fault core and a thicker damage zone where microstructures generated by the stress are present and an undeformed host rock that does not show tectonic-related microstructures.

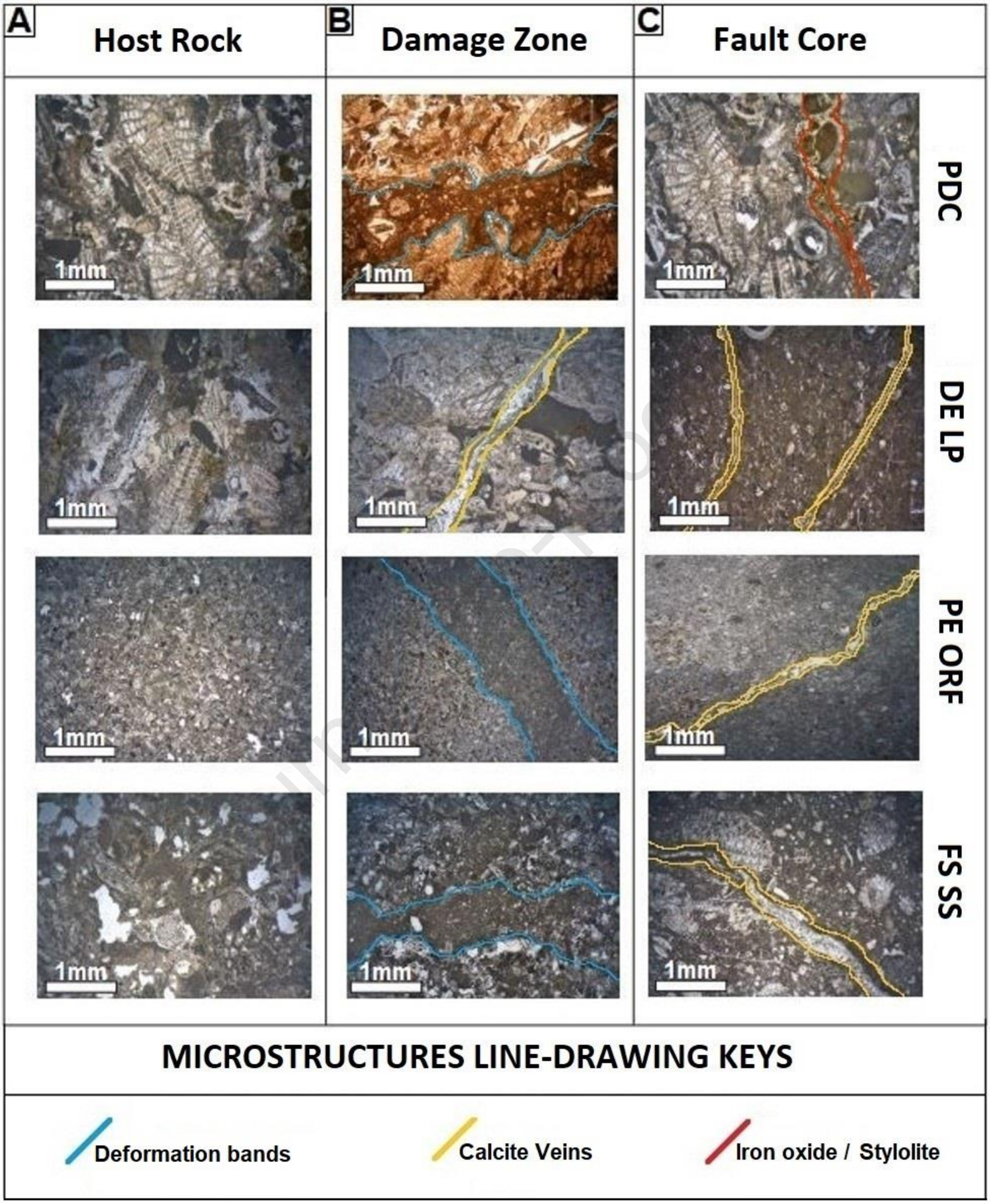

Figure 2. Sampled fault rocks in thin sections belonging to the different analysed faults (PDC, DE LP, PE ORF, FS SS). A) Host rocks samples. B) Damage zone samples. C) Fault core samples. The coloured line drawing represents some relevant microstructural observations. Scale bar = 1 mm.

Host rock

Samples belonging to the host rock appear undeformed and therefore reflect the characteristics of the protolith in which the fault developed (Figure 2A). The host-rock samples belong to the Orfento Formation, to the Lepidocyclina Limestone informal member of the Bolognano Formation and to the Santo Spirito Formation.

- The Lepidocyclina Limestone consists of a rudstone calcarenite in agreement with the classification of Dunham (1962) and Embry and Klovan (1971), whose major microfossils are the larger benthic foraminifera such as lepidocyclinids, rotalids and fragments of non-articulate red algae (PDC and DE LP faults).
- The Orfento Formation is a fine and scarcely cemented grainstone to packstone with clast dimensions up to 2mm (Dunham, 1962; Embry and Klovan, 1971) (PE ORF fault).
- The Santo Spirito Formation is a grainstone-rudstone (Dunham, 1962; Embry and Klovan, 1971) with abundant nummulitids and rotalides larger benthic foraminifera (FS SS fault).

Damage zone

Damage zone samples were collected in an area extending from the fault core up to a distance of about 50 m. These samples typically show deformation structures with a thickness of about 1 mm characterised by clear evidence of grain breakage and grain comminution with no detectable shear offset (Figure 2B). These structures can be referred to deformation bands causing a reduction in porosity, grain fracture and dissolution at grain contact points (cyan line drawing in Figure 2B) (Mollema and Antonellini, 1996; Baud et al., 2004; Fortin et al., 2006; Storti et al., 2007; Wong and Baud, 2009; Fossen et al., 2011; Heap et al., 2015).

Fault core

This fault portion, which accommodated most of the slip, consists of a narrow zone, (~1–15 - cm thick). Samples of the fault core show brittle deformation structures, represented by fractures where calcite and/or iron oxides re-precipitated (Figure 2C). Veins, filled with calcite crystals, are often present probably originating from fractures in which circulating fluids deposit crystalline material inside (Fossen, 2016). The microscopic morphology of calcite crystals shows a blocky texture characterised by equidimensional and randomly oriented crystals (yellow line drawing in Figure 2). These are syntaxial veins in which the filler minerals are of the same type as the minerals in the host rock (Bons et al., 2012; Fossen, 2016).

4.2 Density

Faults	Fault portion		
	HR - ϱ (g/cm³)	DZ - ϱ (g/cm³)	FC - ϱ (g/cm³)
PDC	2.02	2.25	2.66
DE LP	2.28	2.53	2.58
PE ORF	2.125	2.24	2.26
FS SS	2.1	2.30	2.67
Mean	**2.13**	**2.33**	**2.54**

Table 1. Bulk density (in g/cm³) of samples belonging to the fault core (FC), damage zone (DZ) and host rock (HR).

The density measurements show differences between the samples collected on the fault core, on the damage zone and on the host rock (Table 1). All samples show a very consistent behaviour, with progressively higher density moving from the host rock, through the damage zone, to the fault core, reflecting the deformation-related processes to the fault activity. The standard error calculated for density data is 1.4% for HR samples, 1.7% for DZ samples and 2.7% for FC samples.

4.3 Porosity

The total and effective porosities were then calculated and are reported in Table 2.

Faults	Fault portion					
	HR total φ (%)	HR effective φ (%)	DZ total φ (%)	DZ effective φ (%)	FC total φ (%)	FC effective φ (%)
PDC	25.93	24.84	16.97	16.43	0.73	0.73
DE LP	20.34	20.01	8.90	7.83	5.23	2.18
PE ORF	22.50	22.19	21.63	21.11	18.45	18.20
FS SS	22.63	22.58	15.54	14.96	3.38	2.93
Mean	**22.85**	**22.4**	**15.76**	**15.08**	**6.95**	**6.01**

Table 2. Total and effective porosity (in %) of samples belonging to the fault core (FC), damage zone (DZ) and host rock (HR).

Samples related to the fault core show very low porosity values, exhibiting values even below 1%. Damage zone samples have larger porosity compared to samples collected on the fault core, but it is still lower than the host rock samples. Host rock samples show porosities higher than 20% and the porosity is almost entirely connected.

4.4 Seismic velocity

Seismic velocities of the sampled lithologies, measured at ambient pressure, are reported in Table 3.

Faults	Fault portion								
	HR -Vp (m/s)	HR -Vs (m/s)	HR - Vp/Vs	DZ -Vp (m/s)	DZ -Vs (m/s)	DZ - Vp/Vs	FC -Vp (m/s)	FC - Vs (m/s)	FC - Vp/Vs
PDC	4120	2520	1.63	4410	2620	1.68	5890	3240	1.82
DE LP	3780	2270	1.67	4730	2770	1.71	5400	3080	1.75
PE ORF	3730	2250	1.66	3860	2350	1.64	3950	2420	1.63
FS SS	3820	2350	1.63	4470	2670	1.67	5440	3120	1.74
Mean	**3862**	**2347**	**1.65**	**4367**	**2602**	**1.68**	**5170**	**2965**	**1.74**

Table 3. Seismic velocity of P and S waves (expressed in m/s) and Vp/Vs ratio of the lithologies sampled and characterised belonging to the fault core (FC), damage zone (DZ) and host rock (HR).

The lithologies characterised by higher seismic velocities are the rocks sampled on the fault core. Lower seismic velocities are measured for the rocks related to the damage zone region. As expected, due to the higher porosity, samples with the lowest seismic velocities values are those belonging to the host rock. The standard error, calculated for seismic velocity measurements, ranges between 2.2% and 4%.

5. Model building

A 3D structural model has been first built with Petrel. The 3D volume of the model was divided into a grid with cells size of 10 m^3 similar to Janson et al., 2007 and Janson et al., 2011. Topography was modelled from a DEM while formation tops were inferred using public well data (ViDEPI Project, 2012; Tomassi et al., 2022).

The number of zones of the 3D model reflects the petrophysical zones, identified by Tomassi et al. (2022) and follows the regional stratigraphy (Ghisetti and Vezzani, 2002; Di Luzio et al., 2004; Videpi, 2012; Brandano et al., 2016). From bottom to top, these petrophysical zones are: the Orfento Formation (ORF), Santo Spirito Formation (SS), Lepidocyclina Calcarenites (LP), Hemipelagic Marls (HM), Lithotamnion Limestones (LL) and the flysch cover (FC) (Figure 3A).

Thanks to the property modelling tool, it was possible to distribute the petrophysical data measured in the laboratory into the petrophysical zones (i.e., the Lithologic Units ORF; SS; LP; HM; LL; FC) using the User Defined algorithm (UD) (Tomassi et al., 2022). With the UD algorithm, each zone was populated with constant interval velocities (Figure 3B).

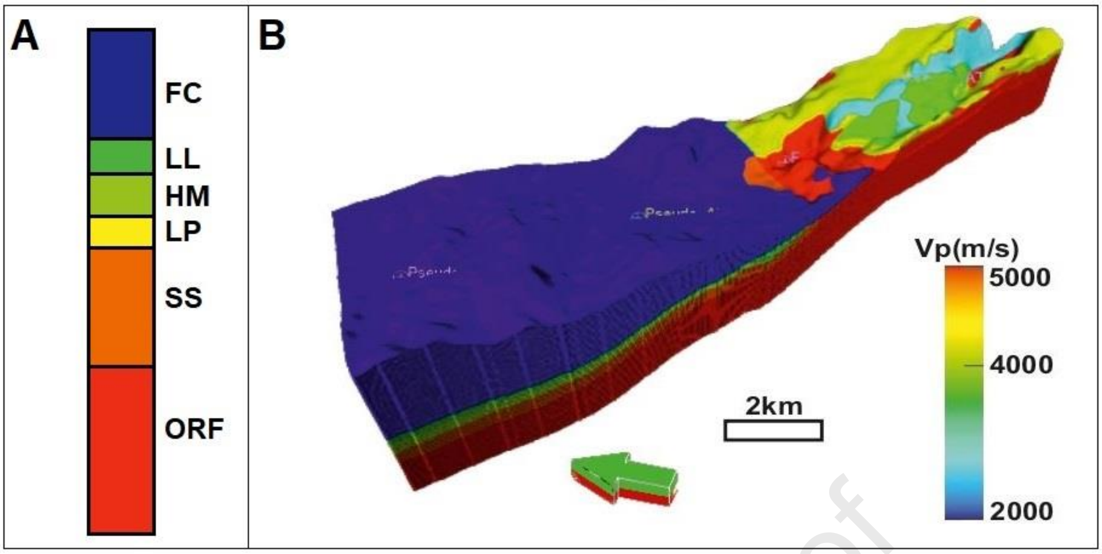

Figure 3. A) Petrophysical zones modelled to build the Petrophysical 3D model. B) 3D model built with constant interval velocity values within each petrophysical zone of the model volume.

Then, the facies heterogeneity was simulated by using the "SGS Co-Kriging (SGS-CK)" algorithm (Vo Thanh and Lee, 2021; Tomassi et al., 2022) (Figure 4) providing heterogeneous velocity values for each layer (petrophysical zone) of the model.

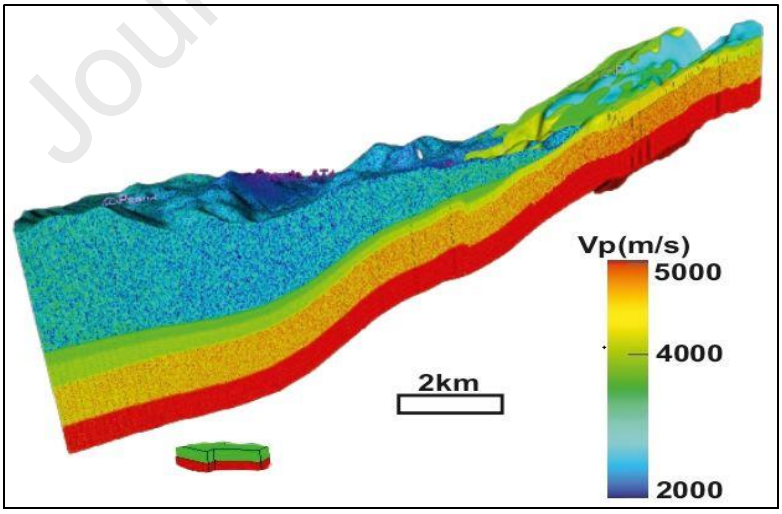

Figure 4. 3D seismic velocity model built with heterogeneous velocity values within each petrophysical zone of the model volume.

2D section generation

A 2D section was extracted from the 3D model (light blue line in Figure 1), using the Petrel calculator tool. The section was then converted into points where each point has three values, representing horizontal distance (x), depth (z) and Vp. Accordingly, the point values were extracted as a spreadsheet. Through a script in Matlab, the spreadsheet was converted into a matrix of Vp values building a new 2D grid, whose samplings are those of the property modelling carried out in Petrel, i.e., 10 m^2. Firstly, a section with constant interval velocities was extracted from the UD algorithm model (Figure 5).

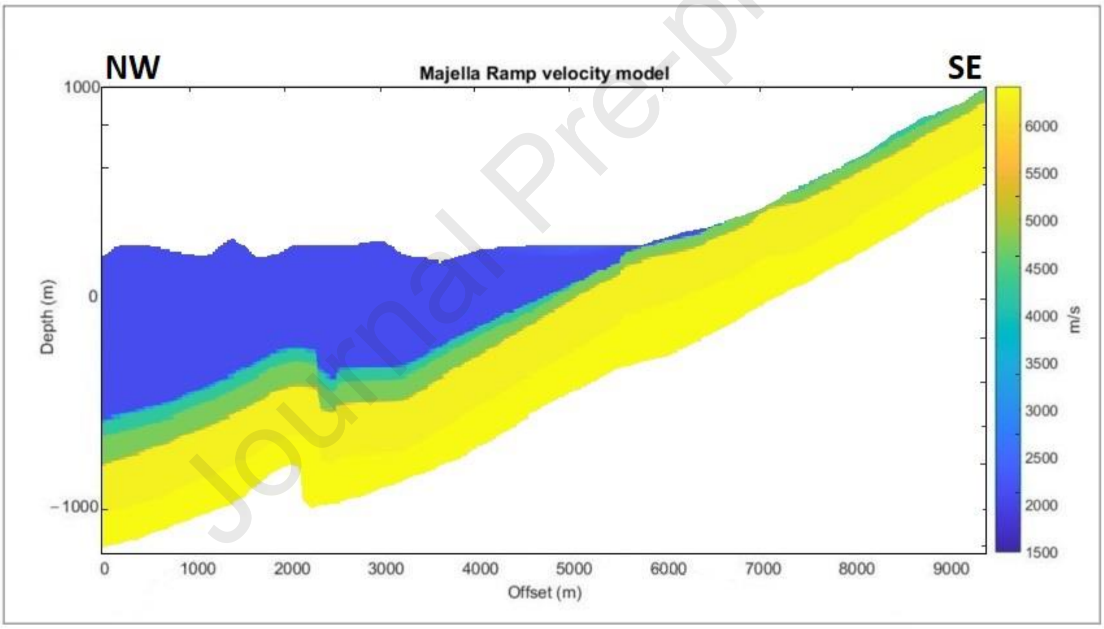

Figure 5. 2D section extracted from Petrel characterised by constant interval velocities.

Subsequently, the section from the SGS-CK algorithm model was extracted. In this way, it has been possible to reproduce the geological seismic velocity model characterised by facies heterogeneity and use it as input data in Matlab. The velocity matrix (shown in Figure 6A) was then used as the velocity model needed to run the synthetic seismic unmigrated stacked section. (De Franco et al., 2019; Tomassi et al., 2022). Furthermore, it should be emphasised that the velocity model was directly based on the experimental velocities of the lithologic units measured at different physical-mechanical states (i.e., HR, DZ and FC) and not derived from a rock-physics-model which considers the physical-mechanical properties (i.e., velocities predicted by the elastic parameters in a physical model).

In this paper, the petrophysical characteristics of rocks adjacent to faults, crossed by the section, were investigated in more detail to evaluate the seismic signature of carbonate-bearing fault zones. In particular, two south-east dipping normal faults are visible cutting the entire carbonate succession excluding the flysch cover (Figure 6). These high-angle faults observed in the section are steep as several shallow normal faults in many sedimentary basins. (Faleide et al., 2021). To get a better view of the fault system analysed the extracted section has been zoomed on the fault zone and the vertical exaggeration has been removed (Figure 6B). The modified velocity model has then been run in Matlab to generate the synthetic seismic fault model.

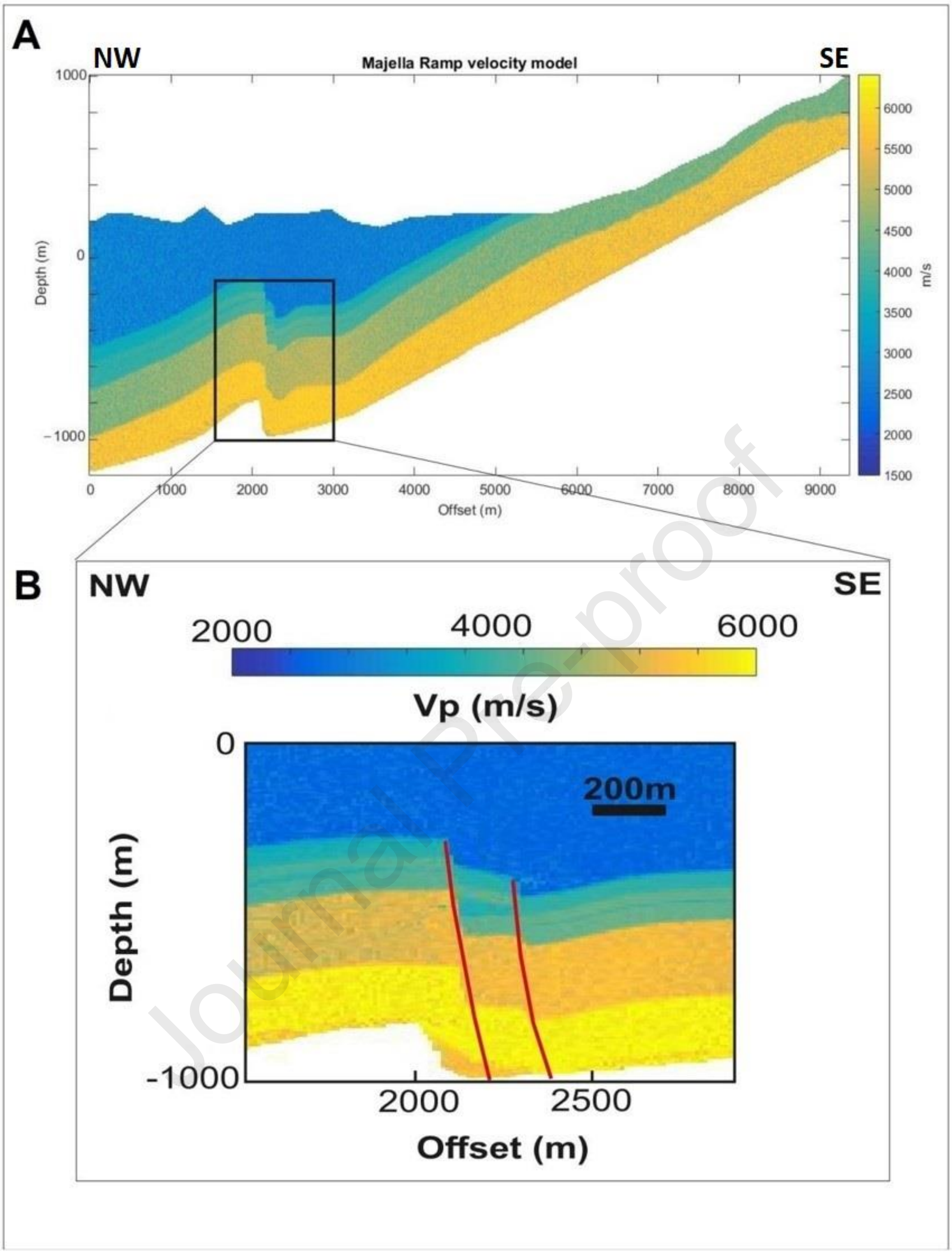

Figure 6. A) 2D model of seismic velocity exported from the Petrel and used as input in Matlab. B) Detail on the fault system without vertical exaggeration.

6. Forward modelling

In this work, the finite-difference (FDM) time-domain method was chosen, which is a computational technique applicable to architecturally complex geologic media commonly used for seismic structural modelling (Moczo et al., 2007). Differently from the ray tracing method, in which a significant amount of scattered power from surfaces is not considered (Wang et al., 2002), the finite difference time domain method calculates the total wavefield. The approach used is a 2D full-wave modelling in which the wavefront is mechanically propagated through the modelled structure simulating unmigrated stacked sections.

Seismic processing and migration use reflections to reconstruct subsurface geometry with continuous and pronounced reflectors (Khaidukov et al., 2004). However, the identification of some geological discontinuities, such as faults, simply shows a discontinuity of reflectors (Klokov et al., 2010). The seismic response of faults is recorded in diffractions that are lost during processing and migration, while diffraction analysis can lead to revealing structural information and additional details of the carbonate system (Moser and Howard, 2008).

For these reasons, unmigrated synthetic modelling was used in this work. This allows the diffractive component to be preserved, although this may limit the resolution. It should also be kept in mind that unmigrated stacked sections presented in this work do not coincide with seismic images to be used for interpretation, but for the analysis of the diffraction hyperbolas to obtain further information on deformation behaviour.

To choose the approach for modelling the Majella carbonate ramp, different techniques in the literature were analysed (see par. 1). In order to preserve diffractions, the modelling is pure-acoustic and constant-density, where Vp is the only factor controlling acoustic impedance in a theoretical normal incidence and zero-offset model. The ideal unmigrated stacked sections were produced with the concept of exploding-reflectors. Pure 2D acoustic modelling generates limitations arising from unmigrated stacked sections, leading to images with slightly distorted positions and shapes and a decrease in lateral resolution, but preserving the diffraction hyperbolas generated by the acoustic impedance contrasts at the edge of the fault and on the fault plane as dispersion points that allow the ricker wavefront to diffract. From the velocity model shown in Figure 5, an initial synthetic modelling was carried out at constant interval velocities showing continuous reflectors and a classic 'bow-tie' effect of the fault with the horizontal reflection crossing the fault plane due to the intentional absence of the migration process (Figure 7).

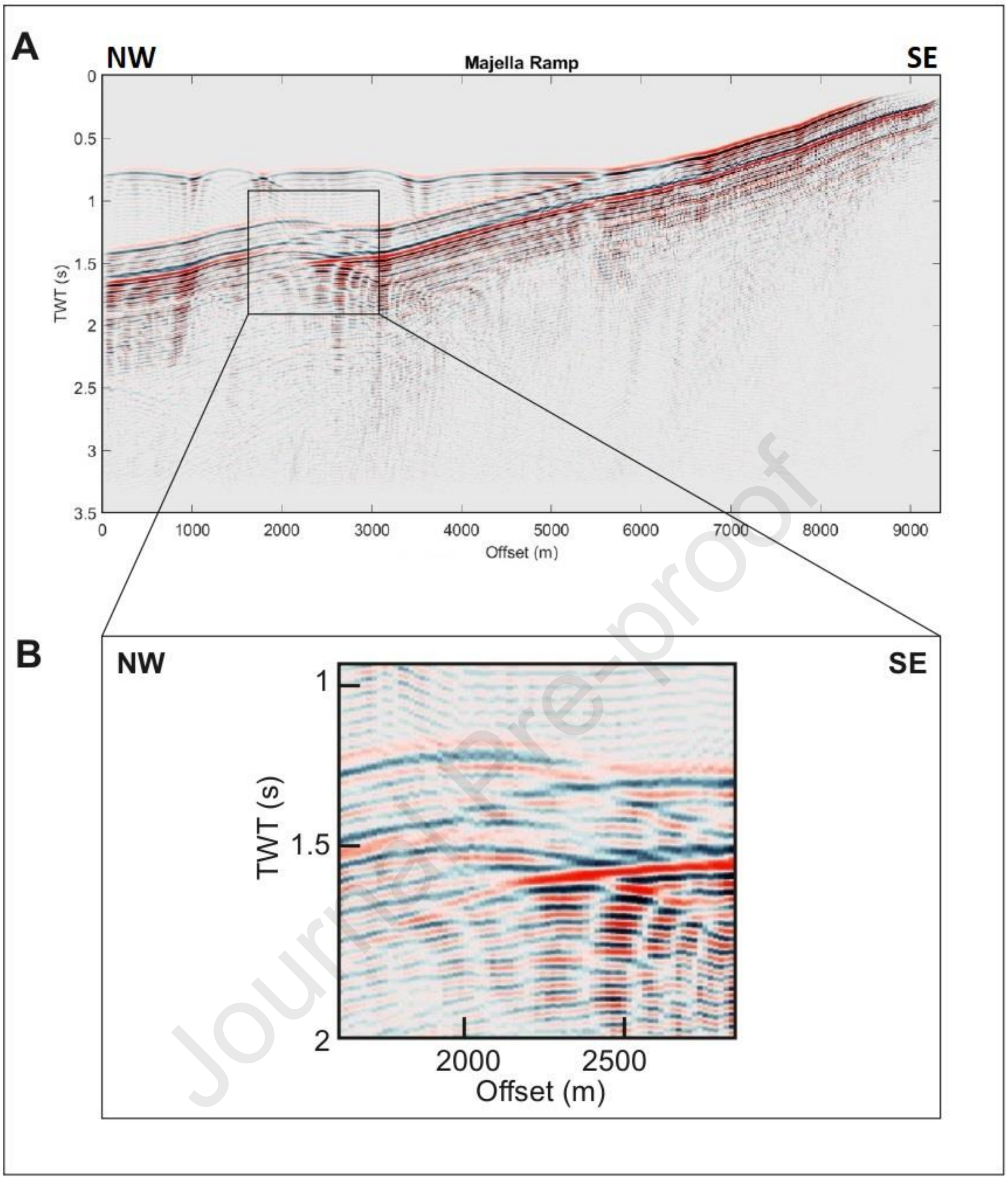

Figure 7. A) Seismic modelling of the Majella carbonate ramp starting from a constant interval velocity model. B) Inset zoomed on the fault zone study object of this work.

In the modelling approach presented in this paper, the seismic signature of facies heterogeneity was additionally introduced (Tomassi et al., 2022). This physical characteristic was modelled using Vp values with a Gaussian distribution range across the petrophysical model layers and not unique and constant values as for classical modelling. The ranges of Vp values, obtained from the laboratory measurements, were derived from the 3D geological model characterised by the SGS-CK algorithm shown in Figure 4 and the 2D section extracted from it was used as the velocity matrix (grid) required for forward modelling (Figure 6). The resulting output shows something similar to background noise that interferes with the display. The genuine heterogeneous facies model represents a perturbed signal affected by constructive and destructive interference generated by the variability of the physical properties of the system showing a complex and perturbed reflection pattern that can be misinterpreted as noise, poor resolution or aliasing. The advantage of modelling facies heterogeneity lies in the fact that the perturbed signal provides additional information on carbonate ramps by representing the physical system more realistically (Tomassi et al., 2022). Consequently, point perturbations with high acoustic impedance were applied to the velocity model, thus using the Ricker wavelet with a perturbative approach to represent petrophysical heterogeneity.

6.1 Fault zone forward-seismic modelling

The presented dataset confirms that fault activity influences the petrophysical characteristics of the surrounding rocks. During the fieldwork, it was mostly recorded a porosity decrease approaching fault planes, however, from a general point of view, the resulting behaviour can be twofold (e.g., Caine, 1996; Michie, 2015; Fossen, 2016) within the study area (Agosta et al., 2009; Giorgioni et al., 2009; Zambrano et al., 2021). On one hand, the movement along the fault can cause fracturing with a consequent increase of porosity and decrease of Vp (Figure 8A). On the other hand, sliding on the fault plane can cause cataclasis and solution/cementation thus deformation bands generating a decreased porosity and consequent increased Vp (Figure 8B) being this typically the case for porous host rocks as observed during the fieldwork.

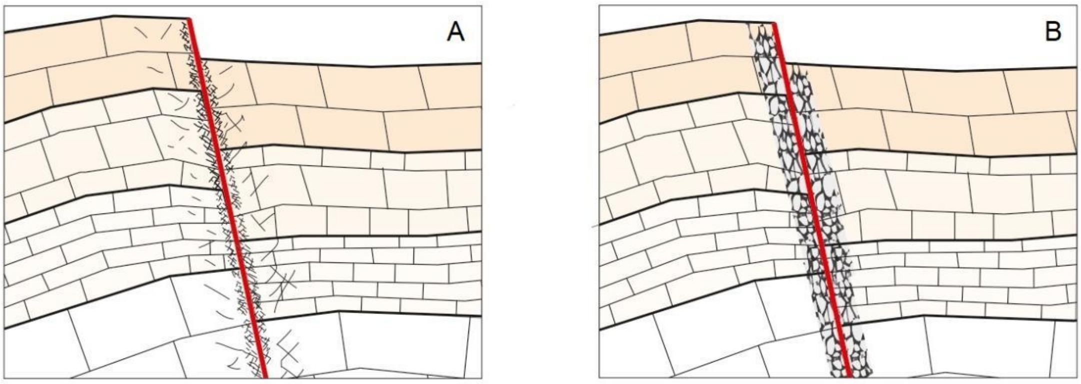

Figure 8. Sketch showing the two end members in accord with the movement along the fault affecting the petrophysical characteristics of the rocks of the damage zone (not to scale). A) Fault causing fracturing, increased porosity and decreased Vp values. B) Fault causing cataclasis and solution/cementation, deformation bands, decreased porosity, increased Vp values.

This twofold behaviour is confirmed by field and laboratory data collected on faults outcropping in the Majella area where examples of both increased porosity (Agosta et al., 2019, Romano et al., 2020) and decreased porosity (this work) damage zones have been observed and characterised.

The measured petrophysical characteristics obviously influence the elastic parameters of the rocks analysed, including the shear modulus. This elastic modulus is a fundamental attribute for the characterisation of damage used to investigate the mechanical properties of geological structures (De Franco et al., 2004). Moreover, the shear modulus is a function of the damage state (Lyakhovsky et al., 1997). Thus, the shear modulus (μ) of the faults covered by this study was calculated using data collected in the laboratory ($\mu = \varrho Vs^2$) to physically investigate the fault zone from an elastic point of view. Figure 9 shows a sharp variation of μ values increasing across the damage zone and the fault core.

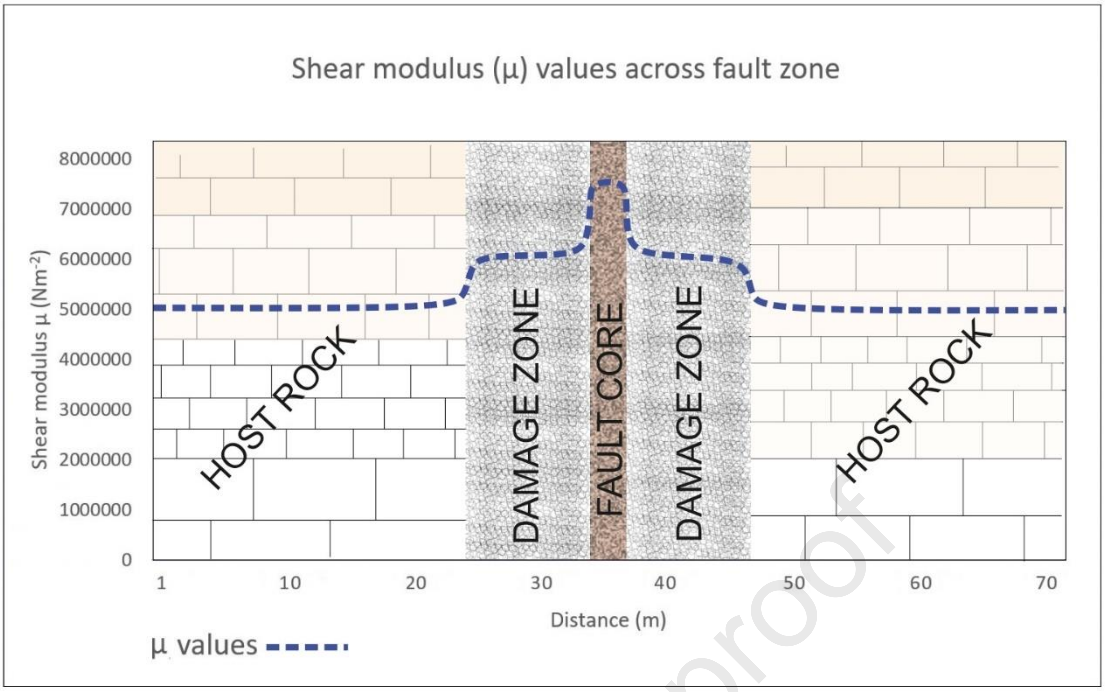

Figure 9. Sketch showing the trend of the elastic modulus (μ) across the fault zone. μ values are represented as a blue dashed line with higher values increasing from the host rock towards the fault core.

The fault zone, characterised by shear modulus variation appears to be formed by three zones (Figure 9). The fault core inner zone is characterised by more competent rocks (relatively high-shear modulus, low porosity and high density); the damage zone is characterised by intermediate μ values; the surrounding host rock zone is characterised by less competent rocks, with relatively low-shear modulus, higher porosity and lower density. The calculation of shear modulus values across the fault confirms, in addition to the petrophysical data, that the structures observed in Majella behave similarly to the sketch shown in Figure 8B.

Consequently the fault zone forward seismic modelling was performed in Matlab following the end members illustrated in Figure 8, analysing the two high angle south-east dipping normal faults buried below a flysch cover that affect the sampled carbonate ramp lithologies shown in Figure 6. Modelling was carried out by decreasing or increasing the Vp values of the damage zone with respect to the Vp values of the host rock. Thus, the first scenario (S1) simulates a damage zone characterised by opening fractures causing increased porosity while the second scenario (S2) simulates a damage zone characterised by the presence of deformation bands or mineralized veins both causing decreased porosity as confirmed by the thin section analysis.

Laboratory measurements of actual fault rocks showed that porosity strongly decreases from the host rock (~23%) to the fault core (~4%); however, the thickness of the fault core is on the order of a few cm and thus not visible at seismic scale. On the other hand, the thicker damage zone still shows a lower porosity value (~17%) if compared to the host rock. Laboratory data show that the recorded change in rock porosity from host rock (23%) to the damage zone (17%) of ~6%, corresponds to a change in Vp of about 500 m/s (Figure 10A). These data are also in agreement with literature data collected on the same lithologies (Ruggieri and Trippetta, 2020). Assuming Vp of 500 m/s lower than that of the host rock (S1) and therefore an increased porosity of 6%, a linear variation between porosity and density results in a decreased density of around 200 Kg/m^3 as shown in the graph in Figure 10B. Consequently, with Vp greater than 1000 m/s compared to those of the host rock (S2) and porosity decreased by 12%, the density is increased by about 400 Kg/m^3.

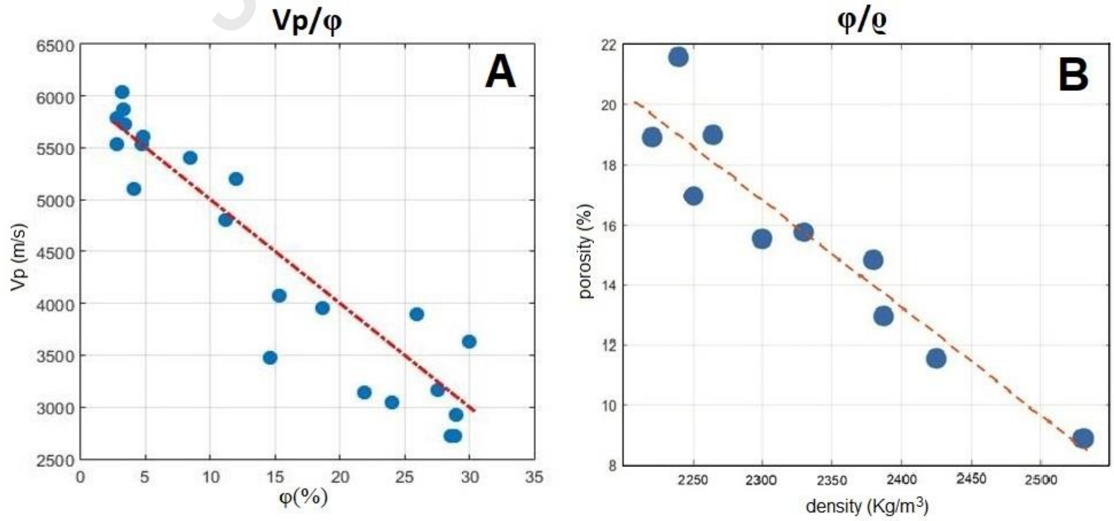

Figure 10. A) Vp versus porosity plot (Vp/φ) showing how porosity varies at different seismic velocities through samples collected in the field and measured in the laboratory. B) Density versus porosity plot (φ/ϱ) showing how density varies for different porosity values through samples collected in the field and measured in the laboratory.

Reflectivity is calculated by the convolution of the wavelet with the reflection coefficient (Rc). Since Rc is controlled by the acoustic impedance (AI) contrasts between two layers in contact ($Rc=AI_2-AI_1/AI_2+AI_1$), the AI of the modelled formations was calculated as the product of their density and their Vp ($AI=\varrho Vp$) both with a not-modelled damage zone, i.e., without changing the petrophysical values according to the end members shown in Figure 8*, and for S1 and S2 (*

Table 4).

Lithologic Units	Not modelled DZ **AI** (MPa s/m^3)	S1 **AI** (MPa s/m^3)	S2 **AI** (MPa s/m^3)
FC	5.7	5.7	5.7
LL	8.18	6.44	12.2
HM	8.97	7.14	13.2
LP	6.78	5.23	10.51
SS	13.41	11.18	18.7
ORF	8.28	6.54	12

Table 4. Acoustic impedances of the modelled formations without modified petrophysical characteristics of the damage zone and according to S1 and S2.

Following the petrophysical results, two velocity models were built (Figure 11). In S1 (Figure 11A), the damage zone is modelled with Vp values 500 m/s lower, thus simulating a 6% increased porosity and decreased density of around 200 Kg/m^3 in the damage zone, for each geologic layer if compared to the host rocks velocity model (Figure 6). In S2, the damage zone is modelled with increased Vp values of 1000 m/s (Figure 11B), thus simulating 12% lower porosity and 400 Kg/m^3 increased density in the damage zone with respect to the host rock. The changes of seismic velocity values in S2 with respect to S1 were voluntarily doubled, to obtain clearly visible results because by increasing Vp values by only 500 m/s, no major changes were visible when compared with the starting unmigrated seismic response at unmodified Vp. The modelled damage zone is 50 m wide from each fault plane in agreement with the field observations.

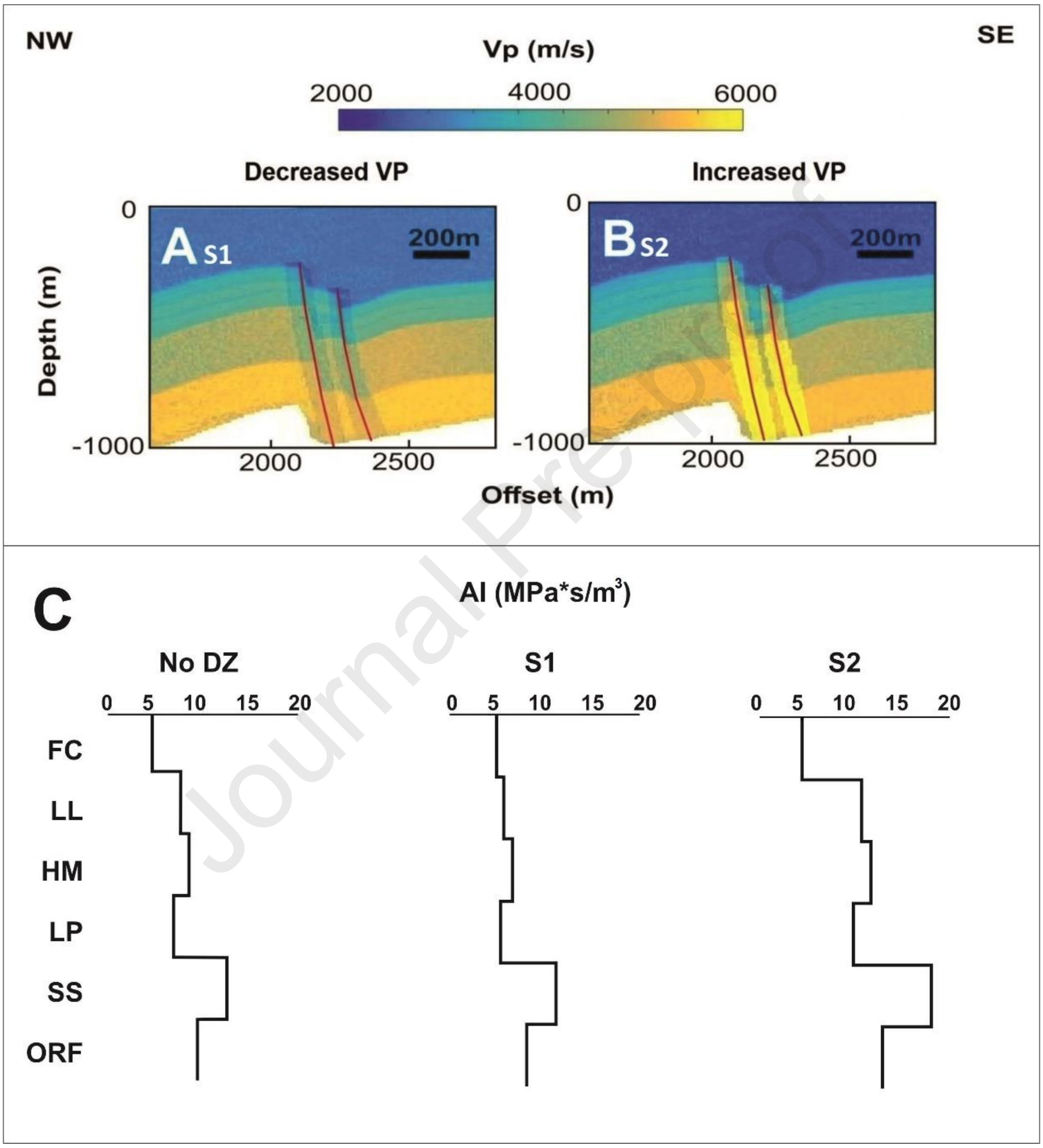

Figure 11. Velocity models with modified Vp values of the damage zone region. A) Damage zone modelled with decreased Vp values when compared to the host rock values (S1). B) Damage zone modelled with increased Vp values when compared to the host rock values (S2). C) Acoustic impedance values of layers with a not-modelled damage zone (No DZ), S1 and S2.

Then, seismic modelling was run on these input models to generate the unmigrated stacked sections with the CREWES consortium toolbox in Matlab (Cho et al., 2007; Margrave and Lamoureux, 2019). CREWES is a set of geophysical codes using the finite difference time domain method. The unmigrated stacked sections were generated using the exploding reflector seismoacoustic approach with the script "*afd_explode.m*" positioning the sources alongside all the reflecting surfaces derived from the input velocity matrix built in the 3D geological model. In this type of modelling, velocity is the only factor controlling the acoustic impedance (De Franco et al., 2019; Tomassi et al., 2022). The modelling parameters required by the script were the input velocity matrix, the sample interval, the grid sampling, the size of the time step for modelling, the maximum time of the seismograms, the positions receivers, the wavelet, the Laplacian approximation used for a discretization of the grid points with neighbour points (Patra and Karttunen, 2006). The prestack bin grid, i.e., the size extension of the traces contributing to the CMP or CDP (linear as the model is 2D) in the modelling presented in this paper is identified with the sampling of the grid cell dimensions. Using an exploding reflector approach, it is not possible to compute the traces in a linear interval, as the sections are not generated from the synthetic shots from the surface and relative processing.

Different frequencies were tested for modelling (from 10 Hz to 100 Hz) and the one that returned the best result as a compromise between resolution and signal depth penetration turned out to be 40 Hz. The use of a 40 Hz frequency ensured the vertical resolution of fault zones considering a resolution threshold of $\lambda/4$. If $\lambda=v/f$ then $\lambda/4=v/4f$ and having the modelled rocks an average Vp value of 4466 m/s investigated at a frequency of 40 Hz this results in a vertical resolution of approximately 28 m, slightly more than half the size of the 50-m-wide modelled damage zones. The lateral resolution corresponds to $R \simeq \sqrt{z(\lambda/2)}$ and in this model varies from 104 m in the shallowest portion of the fault zone to 234 m in the deepest portion. The modelled fault zone is characterised by two faults with a damage zone of about 50 m at a distance of about 100 m between them with a total width of the fault zone of about 200 m. Therefore, according to the calculated values, the fault zone is below the lateral resolution threshold for its shallower portion and just above the threshold in the deeper portion and consequently the fault edge area is well resolved in the seismic image but for the portion below 800 m depth, this can't be stated. The used parameters are reported in Table 5.

Input velocity matrix	100x150 cells velocity model
Sample interval	2 ms
Grid sampling	10 m^2
Time step for modelling	0,5 ms
Tmax (maximum depth time)	2,5 sec
Positions receivers	10 m
Waveform and Wavelet frequency	Ricker 40 Hz
Laplacian approximation	9 points

Table 5. Parameters provided in the CREWES' afd_explode script to run seismic modelling.

Following S1 and S2 velocity models, two different unmigrated seismic responses were obtained (Figure 12).

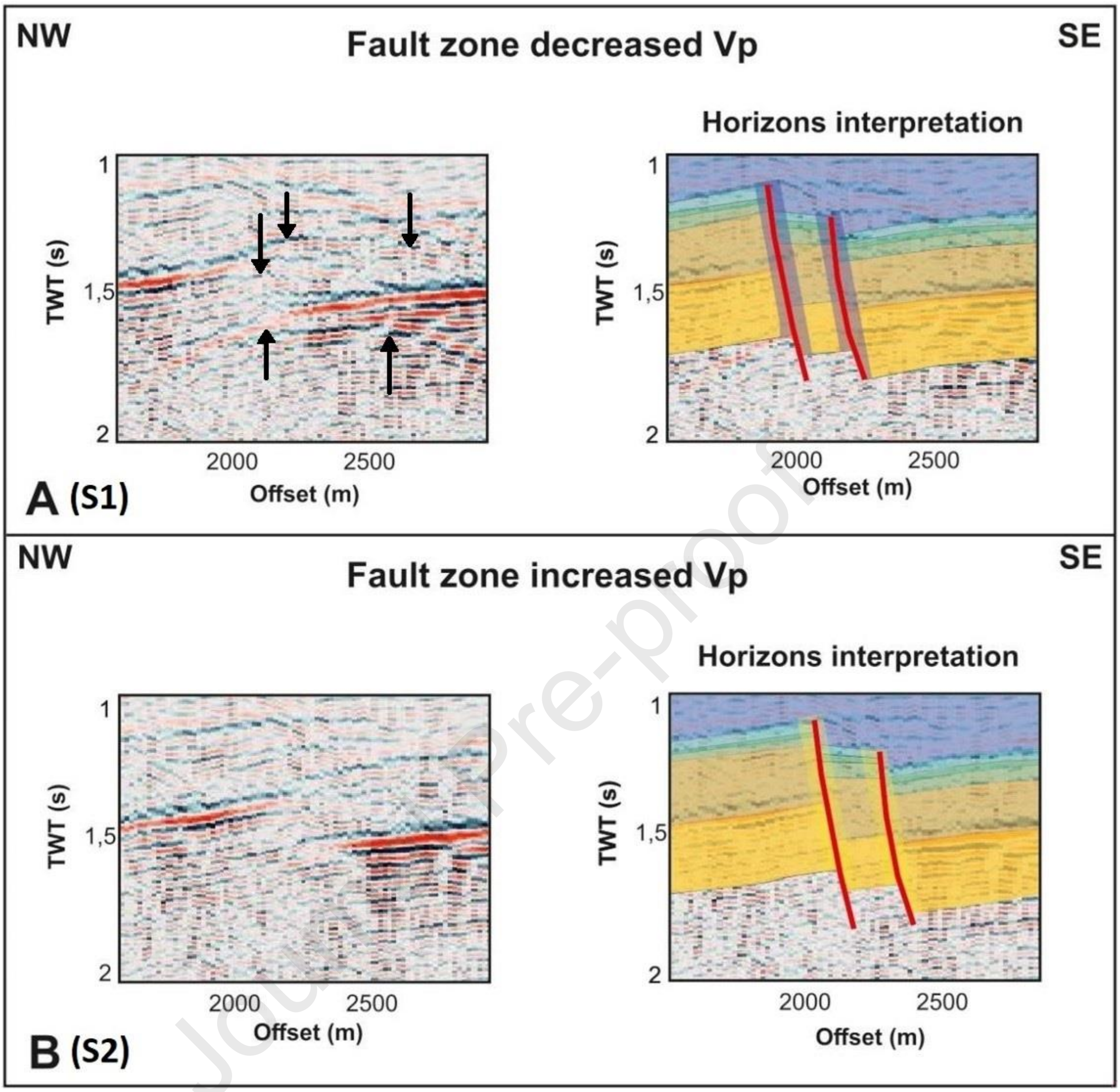

Figure 12. Synthetic seismic (left) and interpretations (right) of the modelled fault zone carried out in Matlab from the velocity models shown in Figure 11. A) S1 model. B) S2 model. The superimposed colours of the petrophysical zones reflect Vp values of the input model in Figure 11. ORF is reported in yellow, SS in light orange, LP in light green, HM in green, LL in cyan, FC in blue. In A (S1) the decreased Vp values damage zone is reported in blue; in B (S2) the increased Vp values damage zone is reported in yellow. Black arrows in S1 highlight the diffraction hyperbolas.

The two unmigrated stacked sections show different seismic responses for the two fault zones (Figure 12). When Vp is reduced (S1, Figure 12A) the damage zone unmigrated seismic response is affected by the presence of diffraction hyperbolas causing a difficult visualization of the faults (Figure 12A left side where black arrows indicate the diffraction hyperbolas). If Vp is increased (S2, Figure 12B) the damage zone unmigrated seismic response does not show appreciable diffraction hyperbolas but a typical reflectors interruption even if the simulated increase in Vp has been doubled with respect to what is reasonably expected. Is to be noted that signal disturbance that might appear aliased or affected by poor resolution is actually caused by the intentionally introduced perturbation representing facies heterogeneity (Tomassi et al., 2022).

6.2 Sensitivity test

Together with the differences in elastic and mechanical parameters between the damage zone and host rock, the dip of the fault plane strongly affects the seismic response (Botter et al., 2014, Iacopini et al., 2016). Moreover, the width of the damage zone, which usually ranges from a few cm to over a 100 m scale, can also affect the results (Caine et al., 1996; Faulkner et al., 2010; Iacopini et al., 2012; 2016). Accordingly, in order to determine which factors mainly affect the observed diffraction hyperbolas, a set of sensitivity tests was performed on a simplified model varying the petrophysical characteristics of the damage zone, the dip of the fault and the thickness of the damage zone.

Figure 13, Figure 14 and Figure 15 show the corresponding simplified models consisting of a flysch layer covering a carbonate host rock in which a fault and its related damage zone are simulated. Bearing in mind that it was designed a model characterised by heterogeneous Vp values distributed in each layer to better simulate the petrophysical heterogeneities in the host rock (Tomassi et al., 2022), velocities were set at 5000 m/s (±500 m/s), simulating carbonates, while for the flysch layer, it was adopted a value of 2000 m/s (±500 m/s). Nevertheless, the modelling results at constant interval velocities were also reported to allow comparison and better understanding what an unmigrated stacked section is (Figure 13A'-B', Figure 14A'-B', Figure 15A'-B').

Following the two end members scenarios S1 and S2 at increased or decreased porosity of the damage zone, the seismic velocities in the damage zone were modelled by assigning velocity ranges from 4000 m/s to 4500 m/s in the S1 scenario (Figure 13A-Figure 14A-Figure 15A) and from 5500 m/s to 6500 m/s in the S2 scenario (Figure 13B - Figure 14B - Figure 15B). Modelling was then started by simulating a 50-m thick high-angle (70°) fault zone based on field observation (Figure 13).

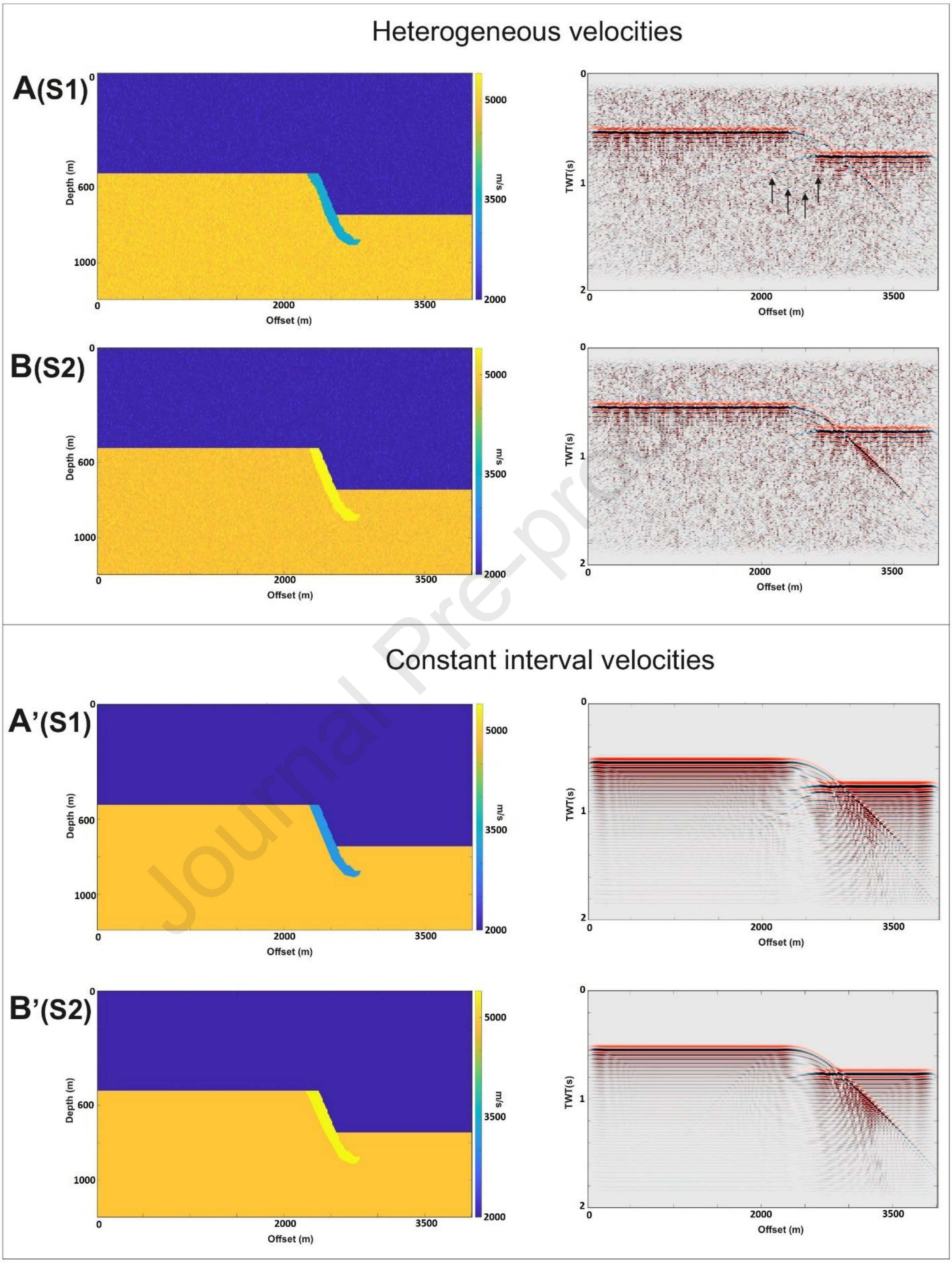

Figure 13. Velocity models and related unmigrated stacked sections created in Matlab to simulate 70° dipping fault zones with a 50-m wide damage zone. A) Fault zone modelled at lower seismic velocities than host rock, simulating an increased porosity damage zone (S1). Black arrows highlight the diffraction hyperbolas. B) Fault zone modelled at higher seismic velocities than host rock, simulating a decreased porosity damage zone (S2). A') S1 fault zone model at constant interval velocities. B') S2 fault zone model at constant interval velocities.

In the unmigrated seismic response of S1, the increased porosity in the damage zone (Figure 13A) is characterised by diffraction hyperbolas in the fault region appearing more chaotic than S2 (Figure 13B). In S1, the hyperbolas are generated by the fault tip and the fault plane acting as point scatterers and causing diffraction of the wavefront. In S2 the seismic image is less characterised by the presence of diffraction hyperbolas. These results reflect the outcomes obtained in the modelling shown in Figure 12 of the two high angle south-east dipping normal faults affecting the Majella carbonate ramp. The branch of the diffraction hyperbola produced by the scattering of the fault tip could be misinterpreted as the upper part of the fault plane although the real signature of the fault plane is below and laterally displaced. However, rather than making the fault plane clearly visible to identify and interpret, the intention is to provide an idea of how modelling an unmigrated stacked section can provide insights about the physical fault system.

Comparing models at heterogeneous velocities with those at constant interval velocities (Figure 13A'-B'), it can be observed that the diffraction hyperbolas developed by modifying the petrophysical characteristics of the DZ in the fault zone are still visible in models with constant interval velocities, especially in S1 (Figure 13A').

Thus, to evaluate what drives the generation of diffraction hyperbolas in the fault zone, the influence of the damage zone width on the unmigrated seismic response was considered. Consequently, the damage zone thickness was expanded in the model up to a thickness of ~100 m maintaining the same dip of 70° (Figure 14).

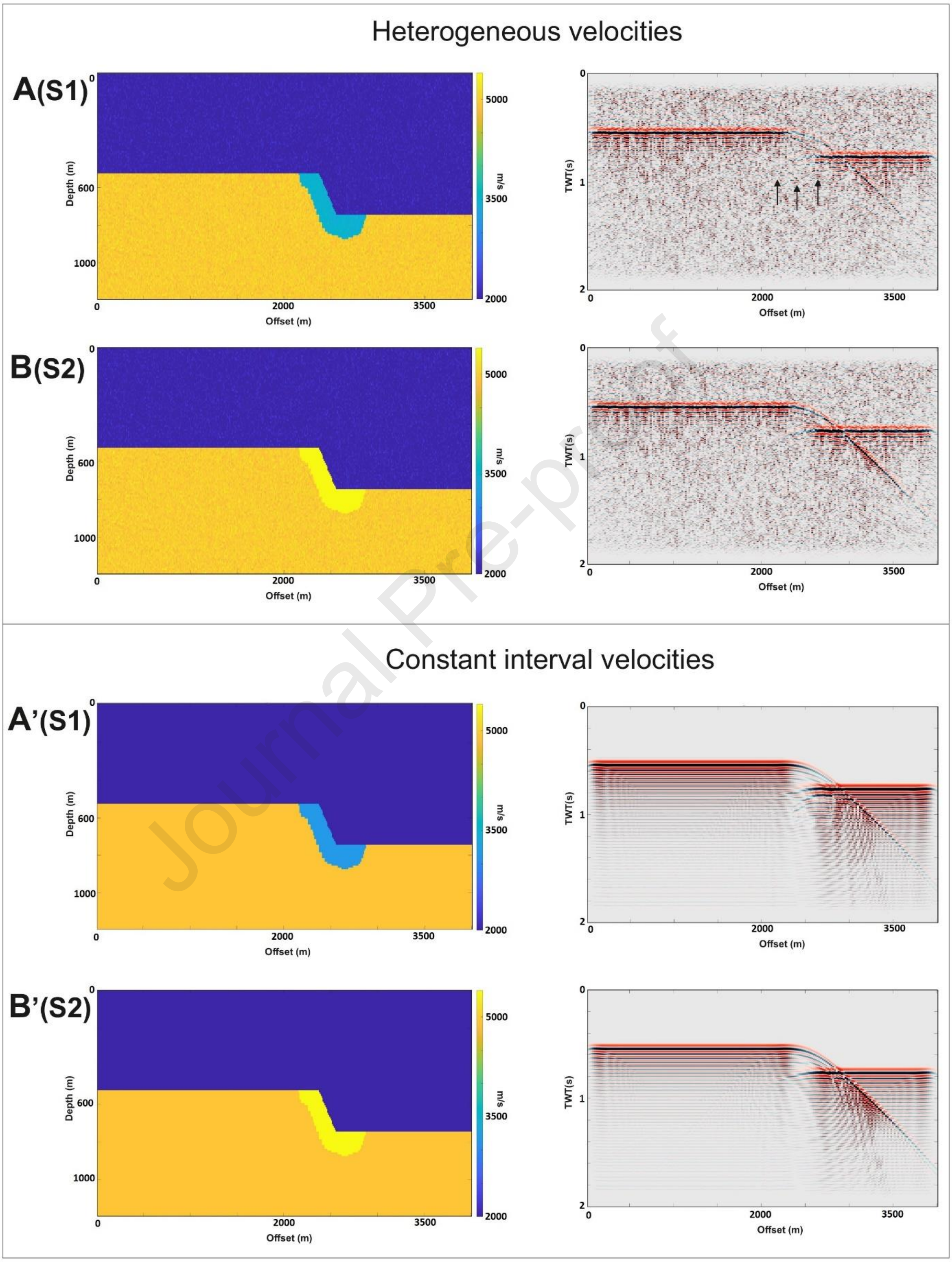

Figure 14. Velocity models and related unmigrated stacked sections created in Matlab to simulate 70° dipping fault zones with a 100-m wide damage zone. A) S1 fault zone model. Black arrows highlight the diffraction hyperbolas. B) S2 fault zone model. A') S1 fault zone model at constant interval velocities. B') S2 fault zone model at constant interval velocities.

The unmigrated seismic response of the ~100-m wide damage zone shows in general less pronounced diffraction hyperbolas than the 50-m wide damage zone. However, the unmigrated seismic response of S1 with a 100-m-width damage zone (Figure 14A), is still characterised by diffraction hyperbolas in the fault region. On the contrary, the unmigrated seismic response of S2 (Figure 14B) is almost free of hyperbolas if compared to the 100-m-width damage zone S1. Even in this test with increased DZ width, the hyperbolas are visible in the constant interval velocity models where a slight diffraction can be observed on the fault in the increased porosity model (Figure 14A'). To evaluate the influence of the dip in the generation of diffraction hyperbolas, it was modelled a lower-angle fault dipping 25° maintaining the damage zone width of 50 m (Figure 15) since maximum hyperbolas were generated with this damage zone thickness as shown in Figure 13 and Figure 14.

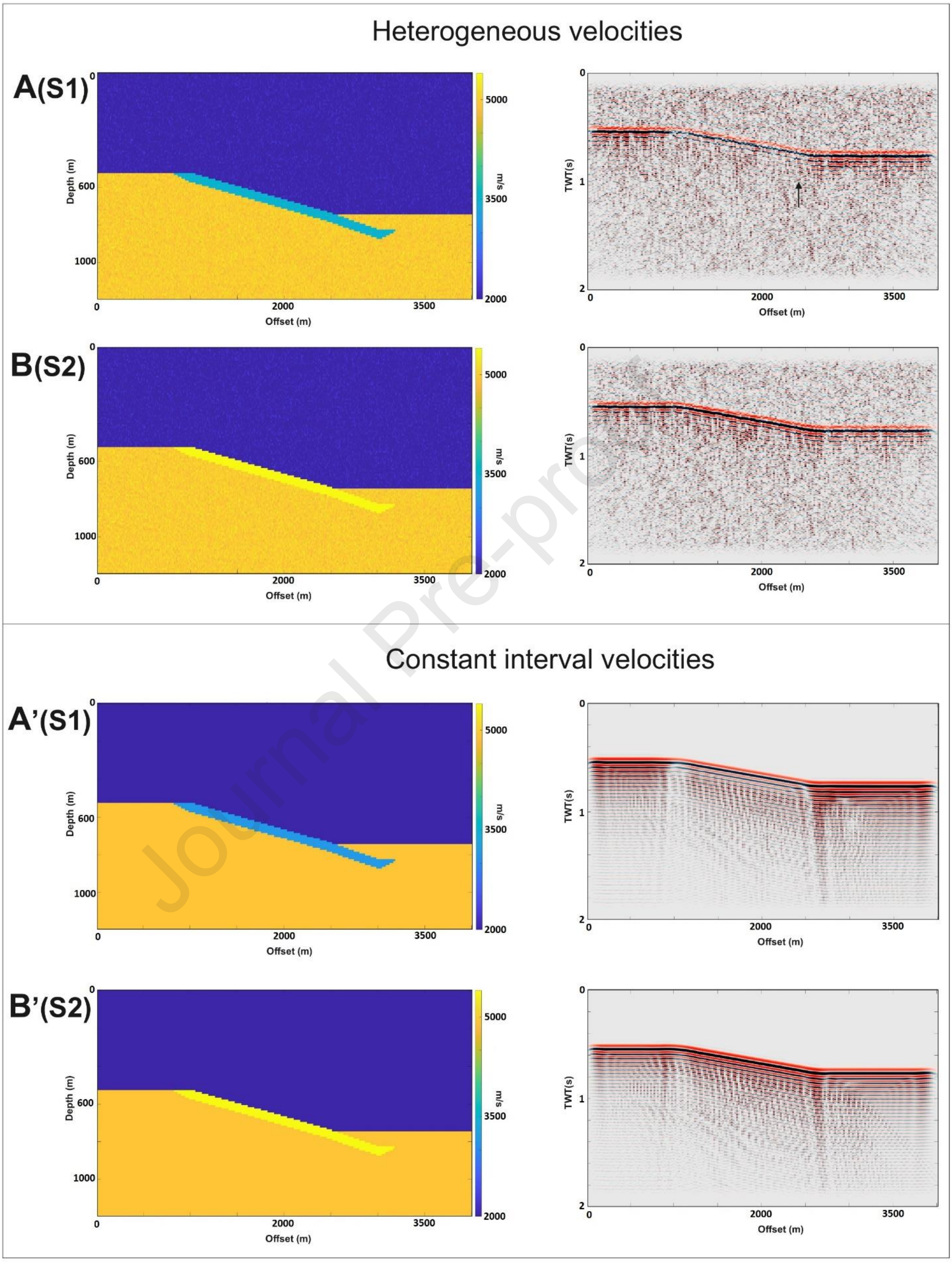

Figure 15. Velocity models and related unmigrated stacked sections created in Matlab to simulate 25° dipping fault zones with a 50-m wide damage zone. A) S1 fault zone model. Black arrows highlight the diffraction hyperbolas. B) S2 fault zone model. A') S1 fault zone model at constant interval velocities. B') S2 fault zone model at constant interval velocities.

The unmigrated seismic response of the model characterised by the 25° dipping fault zone changes considerably. In both these seismic images diffraction hyperbolas are less evident with respect to those related to the 70° dipping fault zones. In particular, the S2 25° dipping fault model (Figure 15B) shows almost absent diffraction hyperbolas compared to the S1 model (Figure 15A). Consequently, the low-angle-dipping fault scenario is the one with the fewest diffraction hyperbolas of the whole sensitivity test. It is worth noting, however, that diffraction hyperbolas are slightly visible at the bottom of the fault in S1 (Figure 15A).

7. Discussions

Field observations integrated by laboratory analyses allowed the characterisation of fault architectures of structures present in the NW sector of the Majella Massif. Many papers emphasise the importance of a detailed petrophysical characterisation to obtain input data for subsequent modelling, and therefore in this work, field and laboratory analysis were combined (Trippetta et al., 2017; Rabbel et al., 2018; Grippa et al., 2019; Trippetta and Geremia, 2019; Ruggieri and Trippetta, 2020; Tomassi et al., 2022; Volatili et al., 2022). This workflow is useful to understand the unmigrated seismic response of stratigraphy affected by structural discontinuities allowing to investigate the seismic signature of the fault zone considering geological and petrophysical aspects (Volatili et al., 2022).

A comparison of measured Vp obtained from laboratory analyses and Vp measured directly in depth shows that the burial process alone does not exert significant control over the increase of Vp values. The increase in Vp caused by mechanical compaction due to burial is weaker than the increase in Vp observed for carbonate rocks characterised by less porosity occluded by diagenesis. Thus, Vp is mainly influenced by diagenetic processes rather than pure compaction during increasing burial depth. Consequently, porosity is the most important physical factor influencing velocity (Eberli, 1997).

The pattern of the shear modulus of the Majella fault zones is well correlated with the damage state of the fault rocks. This is demonstrated by the evidence that μ shows higher values for more competent rocks (e.g., the fault core) and lower values for more porous and less dense rocks (e.g., the host rock). A high shear modulus value records a high state of stress suffered by a rock mass relative to its surroundings, which leads to an increase in normal stress that does not allow fractures to open, leading to an increase in density and seismic velocity (De Franco et al., 2004).

The modification of the petrophysical characteristics of the rocks in the damage zone region, according to the two simulated end members, highlights large differences in the unmigrated seismic response. Marked diffraction hyperbolas in the seismic images of the fault zone area are generated simulating decreased seismic velocity values with respect to the host rock. This scenario simulates decreased seismic velocity due to the presence of fractures-induced secondary porosity (S1) (Giles, 1987). On the contrary, the opposite scenario (S2 with increased Vp values) shows less marked diffraction hyperbolas in the seismic images.

Differently from authors using filters to preserve diffractions and suppress reflections in order to obtain petrophysical information (Bashir et al., 2020), in this work where petrophysics was measured directly in the laboratory, to clearly display the diffraction hyperbolas mathematical differences were made between the seismic outputs (Figure 16). This operation allows the visualisation of the diffractive component created by the variation of petrophysical characteristics in the different fault zone modelling only, blinding the signals of the reflectors by turning them invisible. Thus, from the seismic output without modelled fault zone (i.e., without variation in petrophysical characteristics values in the DZ, used as a benchmark) was subtracted firstly the output of S1 (Figure 16A) and then the output of S2 (Figure 16B).

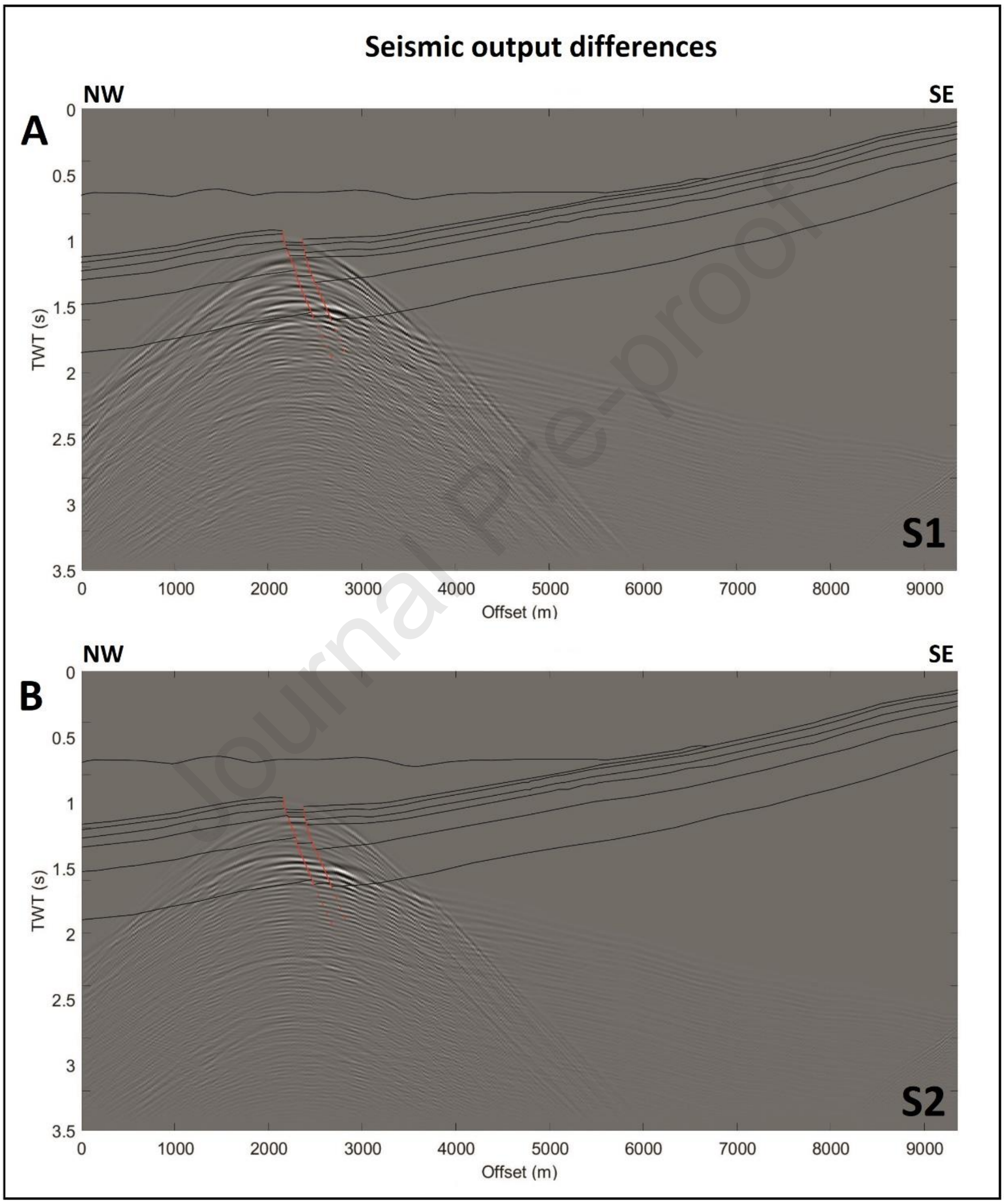

Figure 16. Differences between seismic outputs. A) Difference between the output without variation in petrophysical characteristics values in the DZ and the output with DZ characterised by an increased porosity (S1). B) Difference between the output without variation in petrophysical characteristics values in the DZ and the output with DZ characterised by a decreased porosity (S2).

In Figure 16, the diffractions produced by the different modelling might look similar, but in S1 the amplitudes are clearly greater than in S2. These amplitudes do not allow the hyperbolas in S1 to be camouflaged in the signal furthermore perturbed by facies heterogeneity and characterised by constructive and destructive point interference. On the contrary, hyperbolas produced in S2 characterised by lower amplitudes are masked within the unmigrated seismic response.

Results of the sensitivity test show that the diffraction hyperbolas are increasingly pronounced for steep faults (dip> 60°-70). The test also showed that as the width of the damage zone increases and the dip angle decrease, the hyperbolas gradually become less pronounced. As a result, the hyperbolas are less visible for a damage zone thicker than 100 m and gradually disappear with a dip angle lower than ~25°. However, in all performed tests S1 (increased porosity in the damage zone) always shows detectable hyperbolas, in particular if compared to S2 (decreased porosity in the damage zone).

Lithologies outcropping in the study area show in thin sections the presence of deformation bands and mineralized veins in samples belonging to the fault core and the damage zone, leading thus to a decreasing porosity and increasing density relative to the host rock (Mollema and Antonellini, 1996; Agosta and Aydin, 2006; Rustichelli et al., 2012; Riegel et al., 2019). The presence of this kind of deformation structures is also supported by the petrophysical measurements carried out on the samples, collected on the fault core and on the damage zone. These bands show a lower porosity and higher seismic velocity than the samples collected in the host rock in agreement with literature data (Mollema and Antonellini, 1996; Storti et al., 2007; Fossen et al., 2011; Rustichelli et al., 2012). The deformation-related decrease in porosity is enhanced by the sorting and porosity values of the involved carbonate rocks that are very similar to the porosity of fine to coarse sandstones allowing the development of deformation bands caused by sliding along the fault plane, intensive microcracking and grain comminution (Baud et al., 2004; Baud et al., 2009; Rustichelli et al., 2012; Cilona et al., 2012; Heap et al., 2015). Consequently, the model that most faithfully represents the Majella Massif fault zones is the one represented in Figure 12B. The diffraction hyperbolas in the faults studied in the Majella Massif are barely detectable in the model due to the presence of deformation bands that in this scenario cause a decrease in porosity values of the damage zone with respect to the host rock, while marked diffraction hyperbolas are generated modelling an increased porosity of the damage zone (S1, Figure 12A).

Fracturing associated to fault zones should thus result in evident diffraction hyperbolas on unmigrated seismic images in particular for steep faults with damage zone thinner than ~100 m being this a common architecture for carbonate-bearing faults. Accordingly, in literature several works highlighted diffraction hyperbolas due to the presence of a fault zone where the main driving factor has been related to the geometry of the faults (Liner and Liner 1997; Bano et al., 2002; Pauselli et al. 2010; Ercoli et al. 2012; Ercoli et al. 2013).

The results of this work suggest that the decreased velocity approaching fault is also a leading feature for hyperbolas to develop. Moreover, it is interesting to note that all the cited works analysed shallow context where the low confining pressure allows the fracture to be relatively relaxed bringing an increased porosity in the fractured volume. The results of this work thus suggest that diffraction hyperbolas can preferably be generated by the unmigrated seismic response of fractured and shallow fault systems (Pauselli et al. 2010; Ercoli et al. 2012; Ercoli et al. 2013). This could also explain why seismic images at depth of faulted rock volumes are generally almost free of hyperbolas (Patacca et al., 2008; Bigi et al., 2011; Buttinelli et al., 2021) including in the study area

(Trippetta and Geremia, 2019). On one hand, faults could be characterised by a lower-porosity damage zone as was observed for the studied faults of the Majella area in this study. On the other hand, buried fractured damage zones can be not affected by porosity increase due to the large stress acting at depth that would close the fractures (Trippetta et al., 2017) or to the presence of infill material (Dvorkin and Brevik, 1999; Avseth et al., 2010; Iadanza et al., 2015; Trippetta et al., 2020) counteracting the porosity increase of the damage zone related to fracturing. This possibility is confirmed by a recent study by Volatili et al., 2022 in which it is shown that mechanical fracture opening appears to be a crucial parameter in seismic imaging of buried fault zones affected by high confining pressure. This hypothesis previously formulated in the literature (Nelson and Handin, 1977) argues that lithostatic stress would not allow fractures to open for more than a few microns with lower change in porosity values than those modelled in this study. This is in agreement with laboratory data showing that fractured limestones seal all fractures at 40 ~MPa or ~1.5-2 km depth.

However, it is necessary to specify that the models presented are unmigrated stacked sections and not migrated seismic images to be used for interpretation. In order to analyse these diffractive phenomena, it is necessary to produce a forward modelling exercise with unmigrated stacked sections as this information would be lost in the migration process. By producing or observing migrated sections, the assumptions presented in this paper referred to the stacked sections and not to migration, could not be formulated as there would be no evidence of an increase in porosity of the rocks belonging to the damage zone or anyway the certainty of petrophysical values abrupt variations could not be assured. Consequently, if hyperbolas are not detected in the seismic response of a fault zone it could be due or to an equal or lower porosity of the damage zone rocks compared to those in the host rock or to diffractions suppression through processing. If the diffractive phenomena are detected it could be due to increased porosity of the damage zone rocks and the strength of this model lies precisely in this result.

This work aims to develop a sensitivity to understand the pre-migration model where the "stacked seismic response" guides the geophysicist (more than the interpreter) back to observe a typical diffraction pattern of a given fault with its distinctive petrophysical properties. It is therefore useful to perform forward modelling as it provides these insights.

8. Conclusions

In this work, synthetic seismic images of a faulted carbonate system were developed to investigate the role of the changing petrophysical properties of fault zones in the unmigrated seismic response. The main conclusions are:

- Carbonate fault rocks of the Majella area show a deformation behaviour similar to sandstone and mainly generate deformation bands instead of fracturing due to the high primary porosity. The fractures in the fault core are filled with reprecipitated calcite. These phenomena lead to a progressive decrease in porosity and an increase in seismic velocities approaching fault planes.
- Damage zones with higher porosity and a lower seismic velocity with respect to the host rock, are characterised by seismic images with important diffraction hyperbolas in unmigrated stacked sections. Damage zones with a lower porosity and larger seismic velocity are characterised by seismic images almost free of hyperbolas. The latter model better reflects the behaviour of the faults that are the subject of this study.
- The presence of marked diffraction hyperbolas in the unmigrated stacked sections of a fault zone is strictly related to the increase in porosity of the damage zone rocks with

respect to the host rock. Other factors, such as the geometry of the fault or the thickness of the damage zone, can enhance or reduce the hyperbolas. The analysis of migrated seismic images would not ensure evidence of increased porosity of the damage zone due to the deletion of the diffractive component resulting from the processing.

- On unmigrated stacked seismic images, one of the reasons for reduced hyperbolas in faulted rocks at depth, can be related to deformation mechanisms that result in a main decreased porosity of the damage zone for porous rocks and to the confining stress or infilling material that counteract the fracture-related porosity increase for tight rocks.

Acknowledgements

Funds used for fieldwork, laboratory work, and the writing of this paper were provided by Sapienza University. Mathworks (TM) is thanked for the academic license of Matlab. The CREWES consortium is acknowledged for providing the useful codes needed for the Matlab modelling. Sabina Bigi is thanked for helpful discussion on early versions of the paper. The academic license of the Petrel software was provided by Schlumberger Italiana S.p.A. The two reviewers David Iacopini and Isabelle Lecomte and the editor Fabrizio Agosta are warmly thanked for their valuable revisions, recommendation and suggestions that significantly improved the quality of the work.

References

Aagaard, B.T., Hall, J.F. and Heaton, T.H., 2001. Characterisation of near-source ground motions with earthquake simulations. Earthquake Spectra, 17(2), pp.177-207.

Accarie, H. and Beaudoin, B., 1988. Dynamique de la transition plate-forme/bassin en domaine carbonaté: le Crétacé supérieur du massif de la Maiella (Abruzzes, Italie). Comptes rendus de l'Académie des sciences. Série 2, Mécanique, Physique, Chimie, Sciences de l'univers, Sciences de la Terre, 307(10), pp.1245-1250.

Agosta, F. and Aydin, A., 2006. Architecture and deformation mechanism of a basin-bounding normal fault in Mesozoic platform carbonates, central Italy. Journal of Structural Geology, 28(8), pp.1445-1467.

Agosta, F., Alessandroni, M., Tondi, E. and Aydin, A., 2009. Oblique normal faulting along the northern edge of the Majella Anticline, central Italy: Inferences on hydrocarbon migration and accumulation. Journal of Structural Geology, 31(7), pp.674-690.

Agosta, F., Alessandroni, M., Antonellini, M., Tondi, E. and Giorgioni, M., 2010. From fractures to flow: A field-based quantitative analysis of an outcropping carbonate reservoir. Tectonophysics, 490(3-4), pp.197-213.

Agosta, F., Ruano, P., Rustichelli, A., Tondi, E., Galindo-Zaldívar, J. and de Galdeano, C.S., 2012. Inner structure and deformation mechanisms of normal faults in conglomerates and carbonate grainstones (Granada Basin, Betic Cordillera, Spain): Inferences on fault permeability. Journal of Structural Geology, 45, pp.4-20.

Antonellini, M., Tondi, E., Agosta, F., Aydin, A. and Cello, G., 2008. Failure modes in deep-water carbonates and their impact for fault development: Majella Mountain, Central Apennines, Italy. Marine and Petroleum Geology, 25(10), pp.1074-1096.

Avseth, P., Mukerji, T., Mavko, G. and Dvorkin, J., 2010. Rock-physics diagnostics of depositional texture, diagenetic alterations, and reservoir heterogeneity in high-porosity siliciclastic sediments and rocks—A review of selected models and suggested work flows. Geophysics, 75(5), pp.75A31-75A47.

Aydin, A., Antonellini, M., Tondi, E. and Agosta, F., 2010. Deformation along the leading edge of the Maiella thrust sheet in central Italy. Journal of Structural Geology, 32(9), pp.1291-1304.

Bano, M., Edel, J. B., Herquel, G., & EPGS class 2001–2002., 2002. Geophysical investigation of a recent shallow fault. The Leading Edge, 21(7), 648-650.

Bashir, Y., Mohd Muztaza, N., Moussavi Alashloo, S.Y., Ali, S.H. and Prasad Ghosh, D., 2020. Inspiration for seismic diffraction modelling, separation, and velocity in depth imaging. Applied Sciences, 10(12), p.4391.

Baud, P., Klein, E. and Wong, T.F., 2004. Compaction localization in porous sandstones: spatial evolution of damage and acoustic emission activity. Journal of Structural Geology, 26(4), pp.603-624.

Baud, P., Vinciguerra, S., David, C., Cavallo, A., Walker, E., & Reuschlé, T., 2009. Compaction and failure in high porosity carbonates: Mechanical data and microstructural observations. Pure and Applied Geophysics, 166(5), 869-898.

Bernoulli, D., 2001. Mesozoic-Tertiary carbonate platforms, slopes and basins of the external Apennines and Sicily. In Anatomy of an orogen: The Apennines and adjacent Mediterranean basins (pp. 307-325). Springer, Dordrecht.

Bianchi Fasani, G., Di Luzio, E., Esposito, C., Martino, S. and Scarascia-Mugnozza, G., 2011. Numerical modelling of Plio-Quaternary slope evolution based on geological constraints: a case study from the Caramanico Valley (Central Apennines, Italy). Geological Society, London, Special Publications, 351(1), pp.201-214.

Bielak, J., Loukakis, K., Hisada, Y. and Yoshimura, C., 2003. Domain reduction method for three-dimensional earthquake modeling in localized regions, Part I: Theory. Bulletin of the seismological Society of America, 93(2), pp.817-824.

Bigi, S., Casero, P. and Ciotoli, G., 2011. Seismic interpretation of the Laga basin; constraints on the structural setting and kinematics of the Central Apennines. Journal of the Geological Society, 168(1), pp.179-190.

Billi, A., Salvini, F. and Storti, F., 2003. The damage zone-fault core transition in carbonate rocks: implications for fault growth, structure and permeability. Journal of Structural geology, 25(11), pp.1779-1794.

Bohlen, T., 2002. Parallel 3-D viscoelastic finite difference seismic modelling. Computers & Geosciences, 28(8), pp.887-899.

Bons, P. D., Elburg, M. A., & Gomez-Rivas, E., 2012. A review of the formation of tectonic veins and their microstructures. Journal of Structural Geology, 43, 33-62.

Botter, C., Cardozo, N., Hardy, S., Lecomte, I., Escalona, A., 2014. From mechanical modeling to seismic imaging of faults: a synthetic workflow to study the impact of faults on seismic. Mar. Pet. Geol. 57, 187–207. https://doi.org/10.1016/j.marpetgeo.2014.05.013

Brandano, M., Lipparini, L., Campagnoni, V. and Tomassetti, L., 2012. Downslope-migrating large dunes in the Chattian carbonate ramp of the Majella Mountains (Central Apennines, Italy). Sedimentary Geology, 255, pp.29-41.

Brandano, M., Cornacchia, I., Raffi, I. and Tomassetti, L., 2016. The Oligocene–Miocene stratigraphic evolution of the Majella carbonate platform (Central Apennines, Italy). Sedimentary Geology, 333, pp.1-14.

Buttinelli, M., Petracchini, L., Maesano, F.E., D'Ambrogi, C., Scrocca, D., Marino, M., Capotorti, F., Bigi, S., Cavinato, G.P., Mariucci, M.T. and Montone, P., 2021. The impact of structural complexity, fault segmentation, and reactivation on seismotectonics: Constraints from the upper crust of the 2016–2017 Central Italy seismic sequence area. Tectonophysics, 810, p.228861.

Caine, J.S., Evans, J.P. and Forster, C.B., 1996. Fault zone architecture and permeability structure. Geology, 24(11), pp.1025-1028.

Carcione, J.M., Herman, G.C. and Ten Kroode, A.P.E., 2002. Seismic modeling. Geophysics, 67(4), pp.1304-1325.

Casabianca, D., Bosence, D. and Beckett, D., 2002. Reservoir potential of Cretaceous platform-margin breccias, Central Italian Apennines. Journal of Petroleum Geology, 25(2), pp.179-202.

Cho, D., Hogan, C. and Margrave, G.F., 2007. Acoustic finite difference parameter analysis and modelling in MATLAB. Crewes Project Report, 19(1), pp.1-7.

Cilona, A., Baud, P., Tondi, E., Agosta, F., Vinciguerra, S., Rustichelli, A., & Spiers, C. J., 2012. Deformation bands in porous carbonate grainstones: Field and laboratory observations. Journal of Structural Geology, 45, 137-157.

Cornacchia, I., Andersson, P., Agostini, S., Brandano, M. and Di Bella, L., 2017. Strontium stratigraphy of the upper Miocene Lithothamnion Limestone in the Majella Mountain, central Italy, and its palaeoenvironmental implications. Lethaia, 50(4), pp.561-575.

Cosentino, D., Cipollari, P., Marsili, P. and Scrocca, D., 2010. Geology of the central Apennines: a regional review. Journal of the virtual explorer, 36(11), pp.1-37.

Crescenti, U., Crostella, A., Donzelli, G. and Raffi, G., 1969. Stragrafia della serie calcarea dal Lias al Miocene nella regione marchigiano abruzzese: Parte II. Litostragrafia, biostragrafia, paleogeografia. Memorie della Società Geologica Italiana, 9, 343-420.

CREWES - Consortium for Research in Elastic Wave Exploration Seismology, CREWES MATLAB Toolbox, University of Calgary, https://www.crewes.org/ResearchLinks/FreeSoftware/.

De Franco, R., Bressan, G. and Gentile, G.F., 2004. Elastic moduli and seismogenic aspects of the Friuli upper crust. Boll. Geof. Teor. Appl, 45(1-2), pp.71-87.

De Franco, R., Petracchini, L., Scrocca, D., Caielli, G., Montegrossi, G., Santilano, A. and Manzella, A., 2019. Synthetic Seismic Reflection Modelling in a Supercritical Geothermal System: An Image of the K-Horizon in the Larderello Field (Italy). Geofluids, 2019.

Denham, L.R. and Sheriff, R.E., 2006. Proceedings Indonesian Petroleum association.

Di Cuia, R., Shakerley, A., Masini, M. and Casabianca, D., 2009. Integrating outcrop data at different scales to describe fractured carbonate reservoirs: example of the Maiella carbonates, Italy. First break, 27(3).

Di Luzio, E., Bianchi-Fasani, G., Esposito, C., Saroli, M., Cavinato, G. P., & Scarascia-Mugnozza, G., 2004. Massive rock-slope failure in the Central Apennines (Italy): the case of the Campo di Giove rock avalanche. Bulletin of Engineering Geology and the Environment, 63(1), 1-12.

Dunham, R.J., 1962. Classification of carbonate rocks according to depositional textures. AAPG Mem., 1, pp. 108–121.

Dvorkin, J. and Brevik, I., 1999. Diagnosing high-porosity sandstones: Strength and permeability from porosity and velocity. Geophysics, 64(3), pp.795-799.

Eberli, G.P., 1997. Sonic velocity in carbonate sediments and rocks. Carbonate seismology, 6, p.53.

Embry A.F. and Klovan. J.E., 1971. “A Late Devonian reef tract on northeastern Banks Island, Northwest Territories”. Bull. Can. Pet. Geol., 33, pp. 730–781.

Ercoli, M., Pauselli, C., Forte, E., Di Matteo, L., Mazzocca, M., Frigeri, A., & Federico, C., 2012. A multidisciplinary geological and geophysical approach to define structural and hydrogeological implications of the Molinaccio spring (Spello, Italy). Journal of Applied Geophysics, 77, 72-82.

Ercoli, M., Pauselli, C., Frigeri, A., Forte, E. and Federico, C., 2013. “Geophysical paleoseismology” through high resolution GPR data: A case of shallow faulting imaging in Central Italy. Journal of Applied Geophysics, 90, pp.27-40.

Esmaeilzadeh, S., Afshari, A. and Motafakkerfard, R., 2013. Integrating Artificial Neural Networks Technique and Geostatistical Approaches for 3D Geological Reservoir Porosity modeling with an Example from One of Iran's Oil Fields. Petroleum science and technology, 31(11), pp.1175-1187.

Faleide, T. S., Braathen, A., Lecomte, I., Mulrooney, M. J., Midtkandal, I., Bugge, A. J., & Planke, S., 2021. Impacts of seismic resolution on fault interpretation: Insights from seismic modelling. Tectonophysics, 816(February), 229008. https://doi.org/10.1016/j.tecto.2021.229008

Faulkner, D.R., Jackson, C.A.L., Lunn, R.J., Schlische, R.W., Shipton, Z.K., Wibberley, C.A.J. and Withjack, M.O., 2010. A review of recent developments concerning the structure, mechanics and fluid flow properties of fault zones. Journal of Structural Geology, 32(11), pp.1557-1575.

Fortin, J., Stanchits, S., Dresen, G. and Guéguen, Y., 2006. Acoustic emission and velocities associated with the formation of compaction bands in sandstone. Journal of Geophysical Research: Solid Earth, 111(B10).

Fossen, H., R. Schultz, and A. Torabi, 2011, Conditions and implications for compaction band formation in the Navajo Sandstone, Utah, J. Struct. Geol., 33(10), 1477– 1490, https://doi:10.1016/j.jsg.2011.08.001

Fossen, H., 2016. Structural geology. Cambridge university press.

Ghisetti, F., & Vezzani, L., 2002. Normal faulting, extension and uplift in the outer thrust belt of the central Apennines (Italy): role of the Caramanico fault. Basin Research, 14(2), 225-236.

Giles, M.R., 1987. Mass transfer and problems of secondary porosity creation in deeply buried hydrocarbon reservoirs. Marine and Petroleum Geology, 4(3), pp.188-204.

Giorgioni, M., Cilona, A., Tondi, E. and Agosta, F., 2011, March. Fault Zone Properties In The Roman Valley Quarry Reservoir Analogue: Insight For Well Logs, Core And Field Data. In Offshore Mediterranean Conference and Exhibition. OnePetro.

Grippa, A., Hurst, A., Palladino, G., Iacopini, D., Lecomte, I. and Huuse, M., 2019. Seismic imaging of complex geometry: forward modeling of sandstone intrusions. Earth and Planetary Science Letters, 513, pp.51-63.

Hadizadeh, J. and Rutter, E.H., 1983. The low temperature brittle-ductile transition in a quartzite and the occurrence of cataclastic flow in nature. Geologische Rundschau, 72(2), pp.493-509.

Heap, M.J., Brantut, N., Baud, P. and Meredith, P.G., 2015. Time-dependent compaction band formation in sandstone. Journal of Geophysical Research: Solid Earth, 120(7), pp.4808-4830.

Iacopini, D. and Butler, R.W., 2011. Imaging deformation in submarine thrust belts using seismic attributes. Earth and Planetary Science Letters, 302(3-4), pp.414-422.

Iacopini, D., Butler, R.W.H. and Purves, S., 2012. Seismic imaging of thrust faults and structural damage: A visualization workflow for deepwater thrust belts. First Break, 30(5).

Iacopini, D., Butler, R.W.H., Purves, S., McArdle, N. and De Freslon, N., 2016. Exploring the seismic expression of fault zones in 3D seismic volumes. Journal of Structural Geology, 89, pp.54-73.

Iadanza, A., Sampalmieri, G. and Cipollari, P., 2015. Deep-seated hydrocarbons in the seep "Brecciated Limestones" of the Maiella area (Adriatic foreland basin): Evaporitic sealing and oil re-mobilization effects linked to the drawdown of the Messinian Salinity Crisis. Marine and Petroleum Geology, 66, pp.177-191.

Janson, X., Eberli, G.P., Bonnaffe, F., Gaumet, F. and De Casanove, V., 2007. Seismic expressions of a Miocene prograding carbonate margin, Mut Basin, Turkey. AAPG bulletin, 91(5), pp.685-713.

Janson, X., Fomel, S., Martinsen, O.J., Pulham, A.J., Haughton, P.D.W. and Sullivan, M.D., 2011. 3-D forward seismic model of an outcrop-based geocellular model. Concepts in Sedimentology and Paleontology, 10, pp.87-106.

Jensen, K., Lecomte, I., Gelius, L.J. and Kaschwich, T., 2021. Point-spread function convolution to simulate prestack depth migrated images: A validation study. Geophysical Prospecting, 69(8-9), pp.1571-1590.

Khaidukov, V., Landa, E. and Moser, T.J., 2004. Diffraction imaging by focusing-defocusing: An outlook on seismic superresolution. Geophysics, 69(6), pp.1478-1490.

Klin, P., Priolo, E. and Seriani, G., 2010. Numerical simulation of seismic wave propagation in realistic 3-D geo-models with a Fourier pseudo-spectral method. Geophysical Journal International, 183(2), pp.905-922.

Klokov, A., Baina, R., Landa, E., Thore, P. and Tarrass, I., 2010, October. Diffraction imaging for fracture detection: Synthetic case study. In 2010 SEG Annual Meeting. OnePetro.

Kosloff, D.D. and Baysal, E., 1982. Forward 59 odelling by a Fourier method. Geophysics, 47(10), pp.1402-1412.

Kosloff, D., Kessler, D., Filho, A.Q., Tessmer, E., Behle, A. and Strahilevitz, R., 1990. Solution of the equations of dynamic elasticity by a Chebychev spectral method. Geophysics, 55(6), pp.734-748.

Lyakhovsky, V., Ben-Zion, Y. and Agnon, A., 1997. Distributed damage, faulting, and friction. Journal of Geophysical Research: Solid Earth, 102(B12), pp.27635-27649.

Lecomte, I., Lavadera, P.L., Botter, C., Anell, I., Buckley, S.J., Eide, C.H., Grippa, A., Mascolo, V. and Kjoberg, S., 2016. 2 (3) D convolution modelling of complex geological targets beyond–1D convolution. First Break, 34(5).

Liner, C. L., & Liner, J. L., 1997. Application of GPR to a site investigation involving shallow faults. The Leading Edge, 16(11), 1649-1651.

Manthena, D.V., Kadiyala, A. and Kumar, A., 2009. Interpolation of radon concentrations using GIS-based kriging and cokriging techniques.

Marchegiani, L., Van Dijk, J.P., Gillespie, P.A., Tondi, E. and Cello, G., 2006. Scaling properties of the dimensional and spatial characteristics of fault and fracture systems in the Majella Mountain, central Italy. Geological Society, London, Special Publications, 261(1), pp.113-131.

Margrave, G.F. and Lamoureux, M.P., 2019. Numerical methods of exploration seismology: With algorithms in MATLAB®. Cambridge University Press.

Matonti, C., Lamarche, J., Guglielmi, Y. and Marié, L., 2012. Structural and petrophysical characterization of mixed conduit/seal fault zones in carbonates: example from the Castellas fault (SE France). Journal of Structural Geology, 39, pp.103-121.

Mayolle, S., Soliva, R., Caniven, Y., Wibberley, C., Ballas, G., Milesi, G. and Dominguez, S., 2019. Scaling of fault damage zones in carbonate rocks. Journal of Structural Geology, 124, pp.35-50.

Mercuri, M., McCaffrey, K.J., Smeraglia, L., Mazzanti, P., Collettini, C. and Carminati, E., 2020. Complex geometry and kinematics of subsidiary faults within a carbonate-hosted relay ramp. Journal of Structural Geology, 130, p.103915.

Michie, E.A.H., 2015. Influence of host lithofacies on fault rock variation in carbonate fault zones: A case study from the Island of Malta. Journal of Structural Geology, 76, pp.61-79.

Michie, E.A.H. and Haines, T.J., 2016. Variability and heterogeneity of the petrophysical properties of extensional carbonate fault rocks, Malta. Petroleum Geoscience, 22(2), pp.136-152.

Moczo, P., Robertsson, J.O. and Eisner, L., 2007. The finite-difference time-domain method for modeling of seismic wave propagation. Advances in geophysics, 48, pp.421-516.

Mollema, P.N. and Antonellini, M.A., 1996. Compaction bands: a structural analog for anti-mode I cracks in aeolian sandstone. Tectonophysics, 267(1-4), pp.209-228.

Moser, T.J. and Howard, C.B., 2008. Diffraction imaging in depth. Geophysical Prospecting, 56(5), pp.627-641.

Mutti, M., Bernoulli, D. and Stille, P., 1997. Temperate carbonate platform drowning linked to Miocene oceanographic events: Maiella platform margin, Italy. Terra Nova, 9(3), pp.122-125.

Mutti, M., Bernoulli, D., Spezzaferri, S. and Stille, P., 1999. Lower and Middle Miocene carbonate facies in the central Mediterranean: the impact of paleoceanography on sequence stratigraphy.

Myers, D.E., 1984. Co-kriging—New developments. In Geostatistics for natural resources characterisation (pp. 295-305). Springer, Dordrecht.

Nelson, R.A. and Handin, J., 1977. Experimental study of fracture permeability in porous rock. AAPG Bulletin, 61(2), pp.227-236.

Palaz, I., Marfurt, K.J., 1997. Carbonate Seismology, Carbonate Seismology. https://doi.org/10.1190/1.9781560802099

Patacca, E., Scandone, P., Di Luzio, E., Cavinato, G.P. and Parotto, M., 2008. Structural architecture of the central Apennines: Interpretation of the CROP 11 seismic profile from the Adriatic coast to the orographic divide. Tectonics, 27(3).

Patra, M. and Karttunen, M., 2006. Stencils with isotropic discretization error for differential operators. Numerical Methods for Partial Differential Equations: An International Journal, 22(4), pp.936-953.

Pauselli, C., Federico, C., Frigeri, A., Orosei, R., Barchi, M. R., & Basile, G., 2010. Ground penetrating radar investigations to study active faults in the Norcia Basin (central Italy). Journal of applied geophysics, 72(1), 39-45.

Pisani, L., Antonellini, M., D'Angeli, I.M. and De Waele, J., 2021. Structurally controlled development of a sulfuric hypogene karst system in a fold-and-thrust belt (Majella Massif, Italy). Journal of Structural Geology, 145, p.104305.

Pizzi, A., Falcucci, E., Gori, S., Galadini, F., Messina, P., Di Vincenzo, M., Esestime, P., Giaccio, B., Pomposo, G. and Sposato, A., 2010. Active faulting in the Maiella massif (central Apennines, Italy). GeoActa, 3, pp.57-73.

Rabbel, O., Galland, O., Mair, K., Lecomte, I., Senger, K., Spacapan, J.B. and Manceda, R., 2018. From field analogues to realistic seismic modelling: a case study of an oil-producing andesitic sill complex in the Neuquén Basin, Argentina. Journal of the Geological Society, 175(4), pp.580-593.

Riegel, H., Zambrano, M., Balsamo, F., Mattioni, L. and Tondi, E., 2019. Petrophysical properties and microstructural analysis of faulted heterolithic packages: a case study from Miocene turbidite successions, Italy. Geofluids, 2019.

Romano, V., Hyman, J.D.H., Karra, S., Valocchi, A.J., Battaglia, M. and Bigi, S., 2017. Numerical modeling of fluid flow in a fault zone: a case of study from Majella Mountain (Italy). Energy Procedia, 125, pp.556-560.

Romano, V., Bigi, S., Carnevale, F., De'Haven Hyman, J., Karra, S., Valocchi, A.J., Tartarello, M.C., Battaglia, M., 2020. Hydraulic characterisation of a fault zone from fracture distribution. J. Struct. Geol. 135, 104036. https://doi.org/10.1016/j.jsg.2020.104036

Ruggieri, R. and Trippetta, F., 2020. Petrophysical properties variation of bitumen-bearing carbonates at increasing temperatures from laboratory to model. Geophysics, 85(5), pp.MR297-MR308.

Rusciadelli, G., Sciarra, N. and Mangifesta, M., 2003. 2D modelling of large-scale platform margin collapses along an ancient carbonate platform edge (Maiella Mt., Central Apennines, Italy): geological model and conceptual framework. Palaeogeography, Palaeoclimatology, Palaeoecology, 200(1-4), pp.245-262.

Rusciadelli, G. and Ricci, C., 2008. New geological constraints for the extension of the northern Apulia platform margin west of the Maiella Mt. (Central Apennines, Italy). Bollettino della Società Geologica Italiana, 127(3), pp.375-387.

Rustichelli, A., Tondi, E., Agosta, F., Cilona, A. and Giorgioni, M., 2012. Development and distribution of bed-parallel compaction bands and pressure solution seams in carbonates (Bolognano Formation, Majella Mountain, Italy). Journal of Structural Geology, 37, pp.181-199.

Rustichelli, A., Torrieri, S., Tondi, E., Laurita, S., Strauss, C., Agosta, F. and Balsamo, F., 2016. Fracture characteristics in Cretaceous platform and overlying ramp carbonates: An outcrop study from Maiella Mountain (central Italy). Marine and Petroleum Geology, 76, pp.68-87.

Sager, K., Boehm, C., Ermert, L., Krischer, L. and Fichtner, A., 2018. Sensitivity of seismic noise correlation functions to global noise sources. Journal of Geophysical Research: Solid Earth, 123(8), pp.6911-6921.

Scisciani, V., Tavarnelli, E. and Calamita, F., 2002. The interaction of extensional and contractional deformations in the outer zones of the Central Apennines, Italy. Journal of Structural Geology, 24(10), pp.1647-1658.

Smeraglia, L., Trippetta, F., Carminati, E., Mollo, S., 2014. Tectonic control on the petrophysical properties of foredeep sandstone in the Central Apennines, Italy. J. Geophys. Res. Solid Earth 119, 9077–9094. https://doi.org/10.1002/2014JB011221.Received

Storti, F., Balsamo, F. and Salvini, F., 2007. Particle shape evolution in natural carbonate granular wear material. Terra Nova, 19(5), pp.344-352.

Tomassetti, L., Petracchini, L., Brandano, M., Trippetta, F. and Tomassi, A., 2018. Modeling lateral facies heterogeneity of an upper Oligocene carbonate ramp (Salento, southern Italy). Marine and Petroleum Geology, 96, pp.254-270.

Tomassetti, L., Petracchini, L., Brandano, M., Mascaro, G., & Scrocca, D., 2021. Stratigraphical and sedimentological relationships of the Bolognano Formation (Oligocene–Miocene, Majella Mountain, Central Apennines, Italy) revealed by geological mapping and 3D visualizations. GEOLOGICA CARPATHICA, 72(1), 3-16.

Tomassi, A., Trippetta, F., de Franco, R. and Ruggieri, R., 2022. From petrophysical properties to forward-seismic modeling of facies heterogeneity in the carbonate realm (Majella Massif, central Italy). Journal of Petroleum Science and Engineering, 211, p.110242. https://doi.org/10.1016/j.petrol.2022.110242

Tondi, E., Antonellini, M., Aydin, A., Marchegiani, L. and Cello, G., 2006. The role of deformation bands, stylolites and sheared stylolites in fault development in carbonate grainstones of Majella Mountain, Italy. Journal of structural geology, 28(3), pp.376-391.

Tondi, E., 2007. Nucleation, development and petrophysical properties of faults in carbonate grainstones: evidence from the San Vito Lo Capo peninsula (Sicily, Italy). Journal of Structural Geology, 29(4), pp.614-628.

Trippetta, F., Carpenter, B.M., Mollo, S., Scuderi, M.M., Scarlato, P. and Collettini, C., 2017. Physical and transport property variations within carbonate-bearing fault zones: insights from the Monte Maggio Fault (Central Italy). Geochemistry, Geophysics, Geosystems, 18(11), pp.4027-4042.

Trippetta, F. and Geremia, D., 2019. The seismic signature of heavy oil on carbonate reservoir through laboratory experiments and AVA modelling. Journal of Petroleum Science and Engineering, 177, pp.849-860.

Trippetta, F., Ruggieri, R., Brandano, M. and Giorgetti, C., 2020. Petrophysical properties of heavy oil-bearing carbonate rocks and their implications on petroleum system evolution: Insights from the Majella Massif. Marine and Petroleum Geology, 111, pp.350-362.

Trippetta, F., Durante, D., Lipparini, L., Romi, A. and Brandano, M., 2021. Carbonate-ramp reservoirs modelling best solutions: Insights from a dense shallow well database in Central Italy. Marine and Petroleum Geology, 126, p.104931.

Vecsei, A., Sanders, D.G., Bernoulli, D., Eberli, G.P. and Pignatti, J.S., 1998. Cretaceous to Miocene sequence stratigraphy and evolution of the Maiella carbonate platform margin, Italy.

Vecsei, A. and Sanders, D.G., 1999. Facies analysis and sequence stratigraphy of a Miocene warm-temperate carbonate ramp, Montagna della Maiella, Italy. Sedimentary Geology, 123(1-2), pp.103-127.

Vezzani, L. and Ghisetti, F., 1998. Carta Geologica dell'Abruzzo. SELCA: Firenze, Scale: 1: 100.000, 2 Sheets.

ViDEPI Project, 2012. Visibility of petroleum exploration data in Italy. MISE, Ministero dello sviluppo economico DGRME, Società Geologica Italiana, and Assomineraria. https://www.videpi.com/videpi/videpi.asp

Vo Thanh, H. and Lee, K.K., 2021. 3D geo-cellular modeling for Oligocene reservoirs: a marginal field in offshore Vietnam. Journal of Petroleum Exploration and Production Technology, pp.1-19.

Volatili, T., Zambrano, M., Cilona, A., Huisman, B.A.H., Rustichelli, A., Giorgioni, M., Vittori, S. and Tondi, E., 2019. From fracture analysis to flow simulations in fractured carbonates: The case study of the Roman Valley Quarry (Majella Mountain, Italy). Marine and Petroleum Geology, 100, pp.95-110.

Volatili, T., Agosta, F., Cardozo, N., Zambrano, M., Lecomte, I. and Tondi, E., 2022. Outcrop-scale fracture analysis and seismic modelling of a basin-bounding normal fault in platform carbonates, central Italy. Journal of Structural Geology, 155, p.104515.

Wang, Z., Palaz, I. and Marfurt, K.J., 1997. Seismic properties of carbonate rocks. Carbonate seismology, 6, pp.29-52.

Wang, Y., Ge, Q., Lu, W. and Yan, X., 2020. Well-logging constrained seismic inversion based on closed-loop convolutional neural network. IEEE Transactions on Geoscience and Remote Sensing, 58(8), pp.5564-5574.

Wibberley, C.A., Yielding, G. and Di Toro, G., 2008. Recent advances in the understanding of fault zone internal structure: a review. Geological Society, London, Special Publications, 299(1), pp.5-33.

Wong, T.F. and Baud, P., 2009. Grain crushing, pore collapse and strain localization in porous sandstone. Mechanics of Natural Solids, pp.239-254.

Wrona, T., Fossen, H., Lecomte, I., Eide, C.H. and Gawthorpe, R.L., 2020. Seismic expression of shear zones: Insights from 2-D point-spread-function based convolution modelling. Journal of Structural Geology, 140, p.104121.

Zambrano, M., Volatili, T., Mancini, L., Pitts, A., Giorgioni, M. and Tondi, E., 2021. Pore-scale dual-porosity and dual-permeability modeling in an exposed multi-facies porous carbonate reservoir. Marine and Petroleum Geology, 128, p.105004.

Highlights of the manuscript entitled "How petrophysical properties influence the seismic signature of carbonate fault damage zone: insights from forward-seismic modelling".

By Andrea Tomassi, Fabio Trippetta, Roberto de Franco, Roberta Ruggieri.

- We integrated field and laboratory data to carry out 2D forward modeling
- We developed a workflow linking geocellular model and forward seismic modeling
- The deformation behaviour of carbonate fault rocks can generate compaction bands
- Modification of petrophysics in the damage zone leads to different seismic images
- Diffractions analysis can lead to new insights on buried carbonate fault zone

Andrea Tomassi: Conceptualization, Methodology, Software, Data curation, Writing – original draft preparation, Results interpretation, Figures realization. **Fabio Trippetta**: Conceptualization, Methodology, Data curation, Results interpretation, Validation, Reviewing and Editing. **Roberto de Franco**: Conceptualization, Methodology, Software, Results interpretation, Validation, Reviewing and Editing. **Roberta Ruggieri**: Software, Data curation, Validation, Reviewing and Editing.

Declaration of interests

☒ The authors declare that they have no known competing financial interests or personal relationships that could have appeared to influence the work reported in this paper.

☐ The authors declare the following financial interests/personal relationships which may be considered as potential competing interests: